A Global Climatology of Tropical Easterly Wave Diabatic Heating Using Satellite and Reanalysis Data

By Carrie Lewis-Merritt

Submitted to the graduate degree program in Geography and Atmospheric Science and the Graduate Faculty of the University of Kansas in partial fulfillment of the requirements for the degree of Master of Sciences.

_____

Chair: Justin P. Stachnik

_____

Nathaniel A. Brunsell

_____

David B. Mechem

Date Defended: 29 April 2022

The thesis committee for Carrie Lewis-Merritt certifies that this is
the approved version of the following thesis:

A Global Climatology of Tropical Easterly Wave Diabatic Heating Using Satellite and Reanalysis Data

Chair: Justin P. Stachnik

Date Approved: 12 May 2022

Abstract

Tropical easterly waves (TEWs) play a critical role in regulating convection and precipitation across the global tropics. These synoptic-scale features are commonly known to act as seed disturbances for tropical cyclogenesis and serve as an essential component in monsoon precipitation. Since tropical waves such as TEWs are known to produce large amounts of rainfall and diabatic heating that can strongly affect the large-scale circulation and extratropical weather, better understanding the convective behavior of these waves could lead to more accurate weather forecast and global climate models. To help improve our knowledge of a more elusive type of tropical wave, we use satellite and reanalysis estimates of the diabatic heating associated with and specific to TEWs identified by a tracking algorithm based on low-level curvature vorticity.

This study uses the Tropical Rainfall Measuring Mission (TRMM) version 6 convective-stratiform heating (CSH) and spectral latent heating (SLH) orbital products to create a global climatology (1998-2015) of TEW diabatic heating. Additionally, the observed heating is compared to similar terms using the MERRA-2 temperature tendency data. TEW-specific composites of the vertical structure of diabatic heating and its subterms are compared across datasets and across a variety of tropical regions. There are striking differences between the reanalysis and satellite heating with the reanalysis overpredicting the magnitude of heating, especially at low levels. The observed heating profiles show stronger mid-level heating, although both reanalysis and observed heating profiles show increases in mid-level heating for the conditional (i.e., TEW-specific) heating relative to the unconditional background. Similar patterns of top- and bottom-heaviness emerge in two-dimensional composites of TEW latent heating as stronger heating rates and percent contributions to the background are generally higher at 500 hPa than at 850 hPa. Geographic differences in the strength and distribution of

diabatic heating, inter-term and dataset comparison, and preliminary work towards identifying wave-to-wave and seasonal variability are also discussed.

Acknowledgments

I would like to acknowledge Joe Wermter for his help in creating the MATLAB linear interpolation scheme used to regrid the reanalysis data used in this study. I would also like to thank NASA Precipitation Measurement Missions (PMM) project team members Dr. Elinor Martin and Margaret Hollis for providing the TEW tracking database, in addition to their valuable feedback and collaboration throughout the project. Additionally, I'd like to thank NASA PMM project team member Dr. Rachel McCrary for her collaboration, encouragement, and humor.

The original and processed data for this study are stored at a permanent archive at the University of Kansas computing facility and can be made available upon reasonable request of the authors. TRMM/GPM and MERRA-2 data are available from the Goddard Earth Sciences Data and Information Services Center (GES DISC) at https://disc.gsfc.nasa.gov/. This research was partially funded by NASA PMM Grant #80NSSC19K0720.

Thank you to the Department of Geography and Atmospheric Science for the opportunity to further my academic career and to the faculty and fellow students for all of your insight and feedback that inevitably contributed to this work in one way or another. Thank you to my committee members Dr. Nathaniel Brunsell and Dr. David Mechem for their helpful feedback and insight. Thank you to my fellow *Clouds, Climate, and Precip* (CCP) team members Morgan Stessman and Brett Chrisler for their support, encouragement, and friendship over the years. A special thanks to my advisor, Dr. Justin P. Stachnik, for a never-ending list of reasons. To name only but a few: for his guidance, support, and invaluable feedback throughout every part of creating this thesis. Dr. Justin P. Stachnik also deserves a special acknowledgement for his

patience, encouragement, and kindness that made the most challenging parts of the work feel achievable and as something to look back on and be proud of.

I would like to thank my husband and for his continuous unconditional love and support. Lastly, though he has passed, I would like to thank my father, David, for being the first person to believe in me and encourage my scientific curiosity, and for inspiring me to never stop asking "why."

Table of Contents

List of Tables

List of Figures

Chapter I: A Global Climatology of Diabatic Heating in Tropical Easterly Waves

1.1. Introduction

The abundance of heat, atmospheric moisture, cloud cover, and rainfall found in the tropics leads to a weblike response in the global circulation and weather patterns spanning from the equator to the poles. Tropical convective processes have been shown to produce anomalies in latent heating that then induce similar anomalies in the extratropics (Park and Lee 2019). Specific types of tropical convection such as the Madden-Julian oscillation (MJO; Madden and Julian 1971) are known to influence circulation and weather far outside of their tropical source regions through teleconnections in the form of strong convection-induced Rossby wave trains (e.g., Matthews et al. 2004; Seo and Son 2012; Henderson et al. 2016). At longer time-scales, modes such the El Niño-Southern Oscillation (ENSO) have also been shown to have significant extratropical influence through the forcing and propagation of anomalous diabatic heating originating in the tropics via similar subtropical wave trains (e.g., Ryoo et al. 2013; Yang and Hoskins 2016; Wu et al. 2021). Despite the importance of these modes of tropical convection, the MJO remains poorly represented in global climate models (GCMs) and may result in unreliable projections of global climate (Lin et al. 2006; Hung et al. 2013; Henderson et al. 2017). Uncertainty in ENSO also adds bias to GCMs (Lloyd et al. 2012; Bellenger et al. 2014; Samanta et al. 2018).

Due to the complexity of the subgrid-scale processes responsible for clouds and precipitation, tropical convection remains one of the most quintessential challenges in our observational understanding and modeling of the Earth system. As a result, there are innumerable biases in modeled tropical convection and precipitation embedded into numerical weather prediction and GCMs. One notable example includes the underrepresentation of tropical

waves in GCMs (e.g., Hung et al. 2013; Guo et al. 2015). As with the MJO, accurately representing tropical convection and precipitation processes in short- and long-term forecasting has important extratropical effects. Among these, tropical easterly waves (TEWs) are known to influence weather outside of their source region and contain significant bias in GCMs (Tulich et al. 2011; Daloz et al. 2012; Skinner and Diffenbaugh 2013; Martin and Thorncroft 2015).

TEWs are synoptic scale disturbances known for their influence on convection and rainfall across the global tropics. As expected, these waves are characterized by a sequence of enhanced and suppressed convection within cyclonic and anticyclonic vortices as they propagate westward. TEWs exist roughly within the equatorial trade wind belt with a periodicity of 2-7 days and are characterized by a horizontal wavelength between 2000- to 5000 km (e.g., Reed and Recker 1971; Norquist et al. 1977; Thompson et al. 1979). While they are often considered a type of convectively-coupled wave, they do not follow the theoretical dispersion lines of the shallow water equations in the wavenumber-frequency spectra as they are not purely equatorial waves (Matsuno 1966; Wheeler and Kiladis 1999). This may be, in part, why their dynamics, convective processes, and precipitation characteristics across the global tropics are less understood compared to other types of tropical waves.

Historically, the most studied TEWs are those that originate over West Africa and the Northeastern Atlantic, also known as African easterly waves (Burpee 1972; Reed et al. 1977; Norquist et al. 1977). African easterly waves (AEWs) are commonly known to act as seed disturbances for Atlantic tropical cyclones (e.g., Pasch et al. 1998; Thorncroft and Hodges 2001; Chen et al. 2008; Tyner and Aiyyer 2012) and make large contributions to rainfall during the West African monsoon (e.g., Schlueter et al. 2019). Such direct impacts cause them to remain an

active subject of tropical meteorology research, providing numerous studies dedicated to understanding their dynamics, energetics, and precipitation characteristics.

TEWs outside of the West African genesis region are less studied despite their strong influence on convection and tropical precipitation. These waves may act as seed disturbances for tropical cyclones in other basins and influence monsoon precipitation events (e.g., Serra et al. 2008; Ladwig and Stensrud 2009; Pascale and Bordoni 2016). Not only do TEWs propagate across the entire tropics, but they have also been found to develop in-situ in the tropical East and West Pacific and Central America (e.g., Serra et al. 2008; Belanger et al. 2016; Torres et al. 2021). Recent studies have begun to uncover some of the extratropical effects of TEWs. For example, Cheng et al. (2019) found that AEWs can induce subtropical wave trains due to their convective inflow and outflow, demonstrating that easterly waves may have more large-scale effects than previously known. Our current understanding of these kinds of large-scale effects resulting from TEWs is still lacking, especially for those occurring outside of the Northeastern Atlantic and West Africa. Understanding how TEWs differ in their organization and horizontal structure of precipitation across a variety of tropical regions is of particular interest due to its impact on wave dynamics and longevity.

Pioneering work from Reed and Recker (1971) used rawinsonde data to show the heaviest cloud cover and precipitation occurred west of the cyclonic center or trough as TEWs propagated westward across the Northwestern Pacific. More recent studies using outgoing longwave radiation as a proxy for rainfall have identified a strong coupling between convection and propagation such that the cyclonic center of the disturbance moves in tandem with the active convection (Straub and Kiladis 2003; Wu et al. 2012; Lubis and Jacobi 2015). Various modeling studies on the energetics of TEWs in the Western Pacific and North Atlantic have shown that

latent heat release by moist convection is the primary energy source for wave propagation and the structure of potential vorticity (e.g., Tam and Li 2006; Berry and Thorncroft 2012).

It has long been known that latent heat released through phase changes of water is the primary contributor to diabatic heating in tropical cloud clusters and precipitating systems (Riehl and Malkus 1958; Malkus 1962; Yanai et al. 1973; Houze 1982, 1989; Hartmann et al. 1984). Latent heat of condensation makes up the largest portion of total latent heating and tends to peak in the mid- to upper troposphere in most tropical precipitating systems (Yanai et al. 1973). The vertical structure of latent heating can be indirectly measured from variational analysis and budget studies of sounding data (e.g., Lin and Johnson 1996; Johnson and Ciesielski 2000; Schumacher et al. 2007, 2008) for local domains or estimated from satellite data for the global tropics using a combination of sounding data and cloud resolving models (e.g., Tao et al. 1993; 2010; Shige et al. 2004). In general, these studies revealed the heating profile of deep convective rain to be positive throughout the troposphere and the stratiform regions having maximum heating above the freezing level with cooling below.

Considering heating estimates from reanalysis, Hagos et al. (2010) found reanalyses often maximize in the lower-troposphere and include multiple heating peaks for tropical precipitation unlike TRMM-derived estimates that have maximum heating in the mid-troposphere. In addition, there are significant discrepancies in the magnitude of tropical diabatic heating among reanalyses when compared to various satellite retrievals (e.g., Hagos et al. 2010; Ling and Zhang 2013; Tao et al. 2016). Since diabatic heating can be seen as a proxy for rainfall, such significant inter-reanalyses discrepancies are strongly associated with the well-known dilemma of large spreads of tropical rainfall within reanalyses (e.g., Stachnik and Schumacher 2011). While there are many studies that have focused on identifying the dataset and geographic variability found in

tropical diabatic heating, none are dedicated to TEW-specific high density track or genesis regions across the entire tropics.

Given the above, this study will create a global climatology of the horizontal and vertical characteristics of diabatic heating associated with TEWs to better understand their unique convective processes, how they vary between tropical domains, how their diabatic heating is represented in various datasets, and to discover if they are a potential primary supplier of tropical latent heat. Despite their global occurrence, TEWs remain understudied across the full tropics and our knowledge of their relationship to properties of convection remains limited. Studies that do examine precipitation and heating characteristics in TEWs in other regions often concentrate on one domain at a time, which results in different methods or datasets across studies, limiting the ability to make meaningful comparisons. The work resulting from this study will provide a novel systematic comparison of the climatology of diabatic heating, and therefore precipitation characteristics of TEWs occurring in different convective environments using satellite (TRMM/GPM) and reanalysis (MERRA-2) data. Finally, while it is clear that latent heat fuels TEWs, we are also interested in quantifying the amount of latent heat released due to TEWs and determine their contribution to the global background heating.

1.2. Data and Methods

1.2.1. TEW Database

The primary objectives of this work require a database that contains a substantial record of times and locations for TEWs occurring throughout the global tropics. Hollis and Martin (2021) created a global TEW database for 1980-2018 using curvature vorticity maxima derived from MERRA-2 zonal and meridional winds and a tracking algorithm (“TRACK”) created by

Hodges (1995). The following criteria must be met in order for a feature to be considered a TEW: (1) the feature must meet the curvature vorticity threshold of 10^{-5} s^{-1} and a lifetime minima of at least 2-days; (2) the first point in the track must be between 40°S-40°N; (3) the feature must move in a westward direction of at least 15° of longitude; (4) the feature must not be identified as a tropical cyclone by the International Best Track Archive for Climate Stewardship (IBTrACS; Knapp et al. 2010). Features are identified and tracked separately at 850 hPa and 700 hPa, resulting in a large sample of waves, with over 14,000 at 850 hPa and 24,000 at 700 hPa. The majority of the TEW-specific results in this study come from using the TEW tracks identified at 850 hPa, with some discussion of preliminary results for TEW-specific diabatic heating composited from the 700 hPa track database. The climatological distribution of TEWs at 850 hPa shows a tropics-wide occurrence of TEWs and is particularly pronounced in key development regions such as the Pacific and Atlantic Intertropical Convergence Zones (ITCZ) as shown in Fig. 1.1.

While we are interested in observing how TEW-associated diabatic heating varies across all occurrences of TEWs in the global database, our results also focus on the vertical structure of diabatic heating using spatial averages over the following four TEW track high-density regions as identified in previous work (Belanger et al. 2016). The adapted domains include the North Atlantic (NA; 5-25°N, 20-70°W), South Atlantic (SA; 5-25°S, 10°E-70°W), Northeast Pacific (NEP; 5-25°N, 90-140°W), and Southeast Pacific (SEP; 5-25°S, 90-140°W). Fig. 1.2 shows the study domains outlined in black that are superimposed on an observed latent heating climatology where the heating details are provided in the following section.

1.2.2. Observational Heating Estimates from TRMM/GPM

To address the goals and objectives of this project, i.e., analyzing diabatic heating associated with TEWs, we utilize products derived from the 17-year record of the three-dimensional Tropical Rainfall Measuring Mission (TRMM) data. The TRMM satellite was launched in late 1997 with a 350-km orbit inclined 35° to the equator and was later boosted to orbit at 400 km in 2001 (Kummerow et al. 2000). TRMM was decommissioned in April 2015 after the spacecraft depleted its fuel reserves, providing nearly two decades of satellite observations for tropical weather and climate research. TRMM was replaced in 2015 by the GPM Core Observatory satellite to continue the record of three-dimensional tropical precipitation.

The TRMM Precipitation Radar (PR) was an active sensor that obtained high-resolution measurements of the horizontal and vertical structure of radar echoes with a sensitivity of ~18 dBZ. While subject to the same errors in measuring light rainfall as other remote sensing platforms, the TRMM PR has been shown to capture reasonable estimates of light precipitating regions with rain rates of 0.4 mm day^{-1} (Schumacher and Houze 2000). Since the amount of convective and stratiform components of rainfall observed by the TRMM PR can be used to estimate the structure of tropical convection and diabatic heating (e.g., Schumacher et al. 2004), the extensive climatology of convective and stratiform rain fraction measurements from the TRMM PR provides an invaluable opportunity for greater insight on the organization and structure of TEWs across the tropics.

Since diabatic heating cannot be directly measured by satellites it must be derived indirectly by using other measurable atmospheric variables and/or a cloud-resolving model (CRM). Two commonly used algorithms that have been intercompared and validated are the Goddard Convective-Stratiform Heating (CSH; Tao et al. 1993, 2000) and Spectral Latent

Heating (SLH; Shige et al. 2004, 2009). Using TRMM PR surface precipitation rates, amount of stratiform rain, and the type/location of the cloud systems, the CSH algorithm utilizes lookup tables (LUTs) that contain normalized mean diabatic convective and stratiform heating profiles for various geographic locations. These profiles are primarily obtained from the Goddard Cumulus Ensemble (GCE) CRM, but also utilize profiles from various sounding budget studies. The SLH algorithm also uses a CRM, however, instead of using a limited number of heating profiles from LUTs it uses CRM results to generate latent heating profiles that vary continuously with melting layer, precipitation top height, and rain rate (Tao et al. 2010).

In this study we use the gridded, version 6 heating products of 3GCSH and 3GSLH (hereafter CSH and SLH for brevity). These products are available at the 90-minute or orbital timescale and a swath width of ~245 km. The CSH and SLH have a 0.25° and 0.5º spatial resolution, respectively. The vertical grid for each range from 0- to 18-km with 0.25 km spacing. Both products contain the dominant diabatic heating term, latent heating, which is critical to this study. The CSH includes an estimate of the total apparent heat source, *Q1*, following Yanai et al. (1973) and comprises individual terms for latent, radiative, and eddy sensible heating. The SLH meanwhile contains a modified version of the apparent heat source (*Q1R*), which is defined as the difference in the true apparent heat source (*Q1*) and the missing radiative heating (RH) term (i.e., *Q1* – RH).

We define the total diabatic heating (TOT or total heating for brevity) in this study to be a sum of latent, radiative, and sensible heating terms (hereafter referred to as LH, RH, and SH. In this study, the total heating is referring to only the diabatic heat source, i.e., it neglects other energy transfers such as tendency terms and advection. It is important to note that the TOT for SLH results should be interpreted with caution as this product does not account for radiative

heating. Lastly, the CSH and SLH data used in this study do not contain uncertainty estimates. Recent work by Tao et al. (2019) compared CSH heating estimates with model results and found magnitude uncertainties of around 0.5 K day^{-1} in heavily precipitating regions when analyzing local cross-sections in the extratropics. Due to the large spatial and temporal scales used in this study, we suspect that the magnitude of uncertainty in the TRMM heating is likely to be much smaller than found in Tao et al. (2019).

Before investigating the TEW or wave-specific heating identified by the TEW database, we first establish a climatological or unconditional background. We composite all available CSH and SLH orbital data (1998-2015) to construct maps at 850- and 500 hPa of the tropics-wide background latent heating and regional (i.e., spatial) profile averages of the four diabatic heating terms over the aforementioned study domains. We then match the 3-hourly TEW tracks identified at 850 hPa to the CSH and SLH by accumulating the non-missing orbital data within a 500 km radius of the kinematic wave center (i.e., the curvature vorticity maximum or minimum, depending on the hemisphere) using nearest-neighbor matching. We also constrain our composites such that the orbital data must fall within a 3-hour window centered on the time of the observed wave. To create the regional heating profiles, we take the average of all available profiles that were matched to a TEW track within each respective domain. Similar to the 2D maps created for the background latent heating climatology, we also create climatological maps of the average latent heating within 500 km of the TEW kinematic center where the 500 km threshold was determined from a sensitivity study (not shown). Finally, to quantify the impact that the precipitation, and thus latent heating, produced by TEWs has on the climatological background, we calculate the percent contribution of latent heating from TEWs to the

background at 850- and 500 hPa. Details of these calculations are provided in the results section when presented.

1.2.3. MERRA-2 Reanalysis

Since a primary focus of this study is to evaluate how reanalysis data compares to the observed heating, we utilize the National Aeronautics and Space Administration (NASA) Modern-Era Retrospective Analysis for Research and Applications, version 2 (MERRA-2; Gelaro et al. 2017) temperature tendency ("tdt") data. The MERRA-2 temperature tendency terms can be used to investigate the associated TEW heating and obtain the total apparent heat source in a way comparable to the TRMM data. The MERRA-2 temperature tendency data has a total of eight heat-related variables available that represent different physical and dynamical atmospheric processes. The NA regional average profiles of all terms for a test year, namely 1998, are shown in the supplemental analysis (Fig. 2.1). The MERRA-2 heating contains three dominant terms that are most physically similar to those from TRMM including the tendency of air temperature due to moist processes (DTDTMST), radiation (DTDTRAD), and turbulence (DTDTTRB). Following Yanai et al. (1973) and to compare to the available terms from the TRMM heating data, we classify and interpret the above as LH, RH, and SH, respectively. Similar to the CSH described in the previous section, the total apparent heat source (TOT) is defined as the summation of each of the previous terms (LH + RH + SH) so that the physical processes represented in the reanalysis total more closely match the satellite observations. We note that the original total heating from reanalysis (DTDTANA) is comprised of additional processes not represented in the TRMM heating, including temperature tendencies due to friction, dynamics, physics, and gravity wave damping. In addition to these physical processes,

the MERRA-2 total is also comprised of a non-physical adjustment term to account for the assimilated temperature observations. Since the previous physical and non-physical processes are not represented in the TRMM heating our modified total for MERRA-2 is more appropriate for comparison to the TRMM data.

Other data from MERRA-2 include the assimilated meteorological fields ("asm") that are used to transform MERRA-2's vertical pressure grid to a geometric grid using edge geopotential heights and examine how vertical motion (ω) is related to the diabatic heating associated with TEWs. For both "tdt" and "asm" variables, we use 3-hourly instantaneous data from 1998-2015 at 0.5° x 0.625° spatial resolution, spanning 40°S-40°N, and structured with 25 non-uniform pressure levels from 1000-100 hPa. Additional details regarding the pressure to geometric vertical grid transformation are provided in the supplemental text.

The methods and analysis described in the previous section are repeated for the regridded MERRA-2 data, with an additional analysis of vertical velocity from the reanalysis. Since the MERRA-2 and TEW database are both available at 3-hourly resolution and reanalysis does not have missing data (as in the case of the TRMM orbital data), there is a much larger number of samples included in the composites compared to those for the CSH and SLH. For example, in the NA subdomain there are 23,454 wave samples for the full climatology with available MERRA-2 data but only 1,064 waves with matching CSH data. We thus restrict the MERRA-2 heating data in most composites to the times and location that correspond to samples identified by the TRMM heating data. Heating composites using all available MERRA-2 samples are presented in the supplementary section of this thesis.

In addition to the advantage of a continuous record, MERRA-2 has the potential to pick up on a larger number of light precipitating grid points than TRMM. Though the precipitation in

MERRA-2 is a model product and should be interpreted with caution, it is less likely to show a heavy rainfall bias because it has the ability to produce lighter rainfall than could be detected by TRMM. The previous is reinforced by the fact that assimilated state variables that encourage the formation of model precipitation may come from instruments with higher detection sensitivity. In comparison, the lower instrument sensitivity of the TRMM PR more reliably detects heavy than light precipitation causing the TRMM heating products to be more likely dominated by latent heating. Thus, the conditional means from TRMM are more likely to underestimate diabatic heating in light precipitating areas (i.e., where sensible heat and radiative cooling dominate). As with all data types, reanalysis is subject to various known biases such as overpredictions of tropical precipitation (e.g., Hagos et al. 2010; Ling and Zhang 2013). For these reasons, it is important to use caution when comparing reanalysis diabatic heating estimates to TRMM-derived heating estimates. Finally, it is important to note the independence of the reanalysis and observational data used in this study. The assimilated observations used in MERRA-2 come from a variety of ground-based, aircraft, and satellite observations, however, this does not include observations from TRMM (Gelaro et al. 2017).

1.3. Results

1.3.1. Establishing the Climatological Background Diabatic Heating

Before analyzing the conditional diabatic heating associated with TEWs, we establish the characteristics of the unconditional average or background heating. Since latent heating is expected to be the dominant term in the wave-specific diabatic heating, we first show the low- and mid-level two-dimensional latent heating in Figs. 1.2-1.4 for the global background. The global average for each level (μ) is given in the upper-right corner of Figs. 1.2-1.4, which

excludes times of no heating associated with missing data. For the CSH latent heating (Fig. 1.2), there is nearly 40% more heating at 500 hPa compared to 850 hPa and there are major differences in the distribution of latent heating at each level. Relatively small mean heating rates (~2 K day^{-1}) are found over parts of Central and South America and the Maritime continent at 850 hPa (Fig. 1.2a), whereas there is much stronger (>5 K day^{-1}) and more widespread heating across land at 500 hPa (Fig. 1.2b). Tropical phenomena that produce high amounts of rainfall, such as the east Pacific ITCZ, the South Pacific Convergence Zone (SPCZ), the South Atlantic Convergence Zone (SACZ), the west Pacific warm pool, and the tropical rainforests in South America and equatorial Africa are easily identified in Fig. 1.2. The larger values of latent heating found at 500 hPa over the Maritime continent and west Pacific warm pool are indicative of deep convective cloud regimes (Fig. 1.2b).

Similar features are observed in the SLH latent heating (Fig. 1.3), albeit with generally lower magnitudes of latent heating throughout. There is minimal difference in the 850- and 500 hPa domain means (0.9 and 1.0 K day^{-1}) in the SLH unlike the larger differences between levels for the CSH. The SLH heating distributions again show considerable spatial variations with the same pattern in heating over land at 500 hPa as observed with the CSH (cf. Figs. 1.2-1.3). Differences in the strength of heating between the two levels are more dramatic in MERRA-2 with stronger heating occurring at 850 hPa (Fig. 1.4). The domain mean for the MERRA-2 latent heating at 850 hPa is 2.3 K day^{-1} and 1.3 K day^{-1} at 500 hPa. As with the CSH and the SLH, there is more heating over land at 500 hPa than at 850 hPa in MERRA-2. Similar common features of enhanced rainfall and latent heating (e.g., the SPCZ and SACZ) are also identified in MERRA-2 heating. In addition to strongly overestimating the magnitude of heating at lower levels when compared to the CSH and SLH, the MERRA-2 distribution of low-level heating

over subtropical oceans is remarkably different from the patterns of TRMM heating. This discrepancy in the observed and reanalysis latent heating over the subtropical oceans is particularly pronounced in the southern hemispheric domains at 850 hPa. This analysis of unconditional heating suggests we would expect to see stronger heating for MERRA-2 at lower levels in our four domains when examining the regional profiles.

Fig. 1.5 shows the spatially averaged, background latent heating profiles from each dataset for the NEP and NA. It is worth noting that these averages include times of convective suppression and clear sky scenes (as with the previous maps), so the latent heating magnitude is relatively weak. Unsurprisingly, the MERRA-2 maximum heating occurs lower than the observed heating for both domains. The overestimation of the low-level heating in MERRA-2 is particularly pronounced over the NEP (Fig. 1.5a) in excess of 5 K day^{-1}. It is hypothesized that MERRA-2's low level heating bias could be a result the model misrepresenting low-level and maritime clouds. The CSH heating profiles for both domains show stronger mid-level heating than observed in MERRA-2 and the SLH. The SLH heating in the NEP (Fig. 1.5a) is weaker than the MERRA-2 across all levels and has a somewhat trimodal distribution.

The SLH profile in the NA (Fig. 1.5b) shows very little variation in magnitude and shape compared to the corresponding NEP profile (Fig. 1.5a), although it more closely aligns with the MERRA-2 due to the reduced magnitude of heating in the NA. As with the SLH, there is very little geographic variability observed in the CSH heating profiles, although CSH's mid-level bimodal distribution shows slight variation between the two domains, with slightly stronger heating found at ~6 km in the NEP compared to the NA maximum at ~2.5 km. Performance metrics used to evaluate MERRA-2's representation of the observed background latent heating resulted in six out of eight metrics showing that the vertical structure of latent heating in

MERRA-2 matches the SLH more closely than that of CSH. These performance or error metrics are further discussed in the supplemental section of this thesis (Table 2.1).

In addition to the regional background latent heating average profiles, Fig. 1.6 provides a dataset comparison for the remaining diabatic heating subterms comprising the total apparent heat source. The latent heating terms seen in Fig. 1.6 have already been discussed for Fig. 1.5. The additional subterms that make up the total heating include radiative heating (or cooling) and sensible heating for MERRA-2 (Figs. 1.6a-b) and CSH (Figs. 1.6c-d). Since SLH does not include a separate radiative term, it is only appropriate to compare the individual latent (blue) and sensible (green) profiles to the other datasets as its total is different from the total heating in MERRA-2 and CSH. The radiative (red) profiles in Fig. 1.6 show little geographic variability with the exception of the MERRA-2 radiative profile showing slightly stronger (~0.5 K day^{-1}) cooling below 2 km in the NEP (Fig. 1.6a). Similarly, the CSH and SLH sensible (green) profiles show minimal differences between the NEP and NA with a marginally higher magnitude (~1 K day^{-1}) of sensible heating (and cooling) at low levels in MERRA-2 (Figs. 1.6a-b). The NEP total heating (black) profile for MERRA-2 shows mostly weak heating (< 1 K day^{-1}) below ~11 km with a couple of brief instances of weak cooling (Fig. 1.6a). In contrast, the NA total heating (black) profile for MERRA-2 shows mostly weak cooling below ~8 km with weak heating found at the lowest levels (Fig. 1.6b). There are major differences in both magnitude and shape of the total heating (black) profiles between MERRA-2 and CSH likely resulting from MERRA-2's misrepresentation of low-level clouds and latent heating term.

For the regional background total heating profiles, the radiative cooling is largely negated by the latent heating in MERRA-2. The latent heating term meanwhile comprises a larger amount of the total heating for the CSH at mid-levels despite that the background profile

averages may include a large number of non-precipitating samples relative to those identified by the TEW tracks. Further quantitative analysis of the term intercomparison for the NA background is provided in the supplemental analysis (Table 2.2). In general, based on the resulting profiles from Fig. 1.6 and the correlations in Table 2.2, we find that the radiative subterm contributes a significant amount of cooling and the latent subterm contributions are relatively weak when analyzing the unconditional background diabatic heating. Although these profiles are averaged over domains of high TEW track density, there is still an appreciable number of clear sky observations in subtropical subsidence regions and will thus include a large amount of overall radiative cooling with fewer contributions from latent heating.

As a final analysis for the climatological background characteristics, we examine the vertical motion and how it relates to total heating using MERRA-2 (Fig. 1.7). The resulting profiles in Fig. 1.7b shows subsidence (positive omega) in the NA (solid profile) with climatological ascent in the NEP (dashed profile). Because the stronger latent (Figs. 1.6a-b) and total heating (Fig. 1.7a) occurs in the NEP, it is unsurprising that the positive heating profile corresponds to upward motion. The subsidence seen in the NA is likely explained by the stronger radiative cooling combined with weaker latent heating. As previously mentioned, the stronger negative total heating in the NA is likely a result of including times of convective suppression (i.e., subsidence) in the climatological spatial averages. We note that the NEP is not immune to convective suppression, but the stronger latent heating in the NEP demonstrates that there are likely more times of active convection occurring in the NEP background relative to the NA. A similar analysis for the southern hemispheric domains is provided in the supplemental chapter of this thesis.

1.3.2. Climatology of TEW-Specific Diabatic Heating

Fig. 1.8 shows the conditional average heating profiles at the kinematic center of TEWs for the NEP (left panels) and the NA (right panels) when matched to the corresponding diabatic heating from each dataset. The number of samples (*N)* is given in each panel and indicates the number of TEWs matched to non-missing orbital data within the subdomain. The MERRA-2 diabatic heating profiles are only composited for the times and locations of the non-missing CSH data to provide a more fair dataset comparison. Similar wave-specific diabatic heating profiles composited using all available MERRA-2 samples are provided in the supplemental chapter of this thesis. Due to some of the unavoidable limitations of comparing reanalysis and satellite observations, we do not expect to create perfect dataset comparisons but rather provide climatological results that will serve as a critical first step in understanding how the average diabatic heating associated with TEWs is represented in various datasets.

There are striking differences in the conditional profile averages corresponding to the kinematic center of TEWs (Fig. 1.8) and the unconditional profiles that comprise times with and without waves (Fig. 1.6). As expected, there is a notable increase in the magnitude of latent heating for the wave-specific profile averages. Latent heating is three times stronger in the NEP profiles than for the NA in MERRA-2, with a similar geographic variability although less enhancement in the CSH and SLH. Comparing the abscissa for each dataset in Fig. 1.6 with those of Fig. 1.8 shows that the magnitude of maximum latent heating has more than tripled for the wave-specific profiles in MERRA-2 with significant increases in mid-level heating. We surmise that the strengthened mid-level heating is a result of the transition from shallow to more deep convection and stratiform rain found in the profiles obtained from the TEW kinematic center.

Similar increases in mid-level heating are also observed in the CSH and SLH wave-specific profiles. For the CSH, the magnitude of the conditional latent heating maximum in the NEP (Fig. 1.8c) is about five times stronger than the corresponding unconditional maximum in Fig. 1.6c. The heating magnitude is meanwhile about two and half times greater for the conditional profiles than the background in the NA (cf. Figs. 1.6d and 1.8d). The SLH latent heating maximum increased nearly sixfold in the NEP and more than doubled in the NA (Figs. 1.8e-f). In all datasets, the total heating becomes dominated by the latent heating term with less contribution from the weaker radiative cooling. While the strength of the latent heating has increased significantly for SLH, it is important to note that the latent term is dominant in both Fig. 1.6 and 1.8 due to the missing radiative term. The strength of the sensible heating in each dataset shows minimal increases with the most change observed at low levels in MERRA-2.

Overall, the latent heating term comprises a larger portion of the total heating in Fig. 1.8 than when compared with profiles that include times of convective suppression, such as those obtained from the unconditional regional backgrounds (Fig. 1.6). The previous results are expected as the TEW profiles should contain a significant number of precipitating features where latent heating usually dominates the total heating. While we expect a much larger number of the profiles composited in Fig. 1.8 to come from precipitating grid points at the TEW kinematic center, it is also important to consider that the increases in latent heating might also be muted by including a number of non-precipitating profiles. Since we did not filter out dry TEWs or non-precipitating grid points, it is not guaranteed that the composite profiles are entirely representative of the latent heat release due to precipitation produced in TEWs.

Finally, we again produce regional conditional profile averages from the wave kinematic center for total heating and vertical velocity (Fig. 1.10) to compare to those of the unconditional

regional backgrounds (Fig. 1.7). Both the NA and NEP show strong positive total heating and exceptionally strong upwards vertical motion with negative omega peaks greater than 1 Pa s^{-1}. It is unsurprising that the NEP's larger magnitude of heating corresponds to much stronger upwards vertical motion in the reanalysis where both are about three times stronger than that of the NA. The strong antisymmetry observed in Fig. 1.9 produces a Pearson correlation coefficient, $r = -0.94$ and $r = -0.92$, for the NEP and NA, respectively. The previous further indicates a strong relationship between the wave-specific total (and latent) heating and vertical motion in the tropical subdomains.

1.3.3. TEW Percent Contributions to Background Heating

Before calculating the contribution that TEW-produced latent heating makes to the global background, we first present the conditional average latent heating rates accumulated within a 500 km distance from the TEW kinematic center. The 500 km length was chosen based on a prior series of sensitivity tests using MERRA-2 wave-specific latent heating for a single test year (not shown). The different thresholds tested used a 0-, 100-, 250-, and 500 km distance from the kinematic center of TEWs and showed the most reasonable average latent heating rates for the 500 km accumulation. In addition, TEW precipitation accumulation results from Hollis and Martin (2021) used a 500 km radius for their analysis after determining it was a reasonable radius to capture TEW produced precipitation.

The conditional or wave-specific average latent heating rates for CSH at 850- and 500 hPa are shown in Fig. 1.10. Latent heating accumulated within 500 km of the TEW kinematic center was averaged using the frequency of occurrence of the non-missing CSH data. The global domain means (μ) for each vertical level provided in Fig. 1.10 show that the generally weaker

values of heating (< 5 K day^{-1}) that occur at 850 hPa result in a smaller mean global background (2.3 K day^{-1}) despite more coverage than when compared to the heating at 500 hPa (4.1 K day^{-1}). Conditional latent heating rates at 500 hPa (Fig. 1.10b) show pronounced heating (>7 K day^{-1}) across more confined areas in which deep convection is commonly found (e.g., tropical convergence zones, tropical rainforest regions, surrounding the Maritime continent, and over the west Pacific warm pool region). We also find more accumulated and stronger latent heating where there is a higher density of TEW tracks (Fig. 1.1) including the NEP, West Africa and the NA at both vertical levels.

Aside from slight differences due to different spatial resolutions, the distribution of wave-specific latent heating using SLH in Fig. 1.11 is nearly identical to that of CSH in Fig. 1.10. This result in consistent with expectations since both algorithms use the same TRMM PR data in their retrievals. There are significant differences, however, in the strength of the SLH wave-specific average latent heating as reflected in both the global means (μ) and in the overall distribution of weaker heating rates across the global tropics than when compared to CSH (Fig. 1.10). While the SLH also shows stronger heating at 500- than at 850 hPa, the amount of increase is not as drastic as that observed in CSH. The increase in the global mean from 850- to 500 hPa for CSH is 1.8 K day^{-1}, compared to a 1.0 K day^{-1} increase in SLH. This is consistent with the larger magnitude of conditional average latent heating found in the CSH latent heating profiles (Fig. 1.8) that was also most pronounced at mid-levels when compared to the SLH.

Surprisingly, the differences at 850- and 500 hPa for the MERRA-2 conditional average heating (Fig. 1.12) go against expectations based on the unconditional background heating (Fig. 1.4) and the heating profile averages from the kinematic center (Fig. 1.8). Since the regional latent heating profiles were more bottom-heavy with a positive heating bias at low-levels, it is

interesting to find that there is stronger heating at 500 hPa than at 850 hPa in Fig. 1.12. While the global means show negligible difference (0.2 K day^{-1}), it is evident that there is generally stronger convection, and thus rainfall, produced by TEWs at mid-levels than at lower levels in Fig. 1.12. Similar to some of the differences described above for CSH and SLH, the tropics-wide heating at 850 hPa in MERRA-2 while generally weaker, covers a larger area than observed at 500 hPa. Again, regions known for deeper convection and heavier rainfall have concentrated stronger latent heating rates produced by TEWs in MERRA-2. The differences in low- vs. mid-level latent heating seen in the profile averages taken from the kinematic center and those found by accumulating 2D latent heating within 500 km of the kinematic center further demonstrate that the precipitation associated with TEWs contributes more latent heating at mid-levels, likely resulting from TEW-associated increases in deep convection.

The variation in the strength of conditional latent heating rates among datasets is show in Table 1.1, which provides the NEP and NA domain means. The MERRA-2 domain means contain equal amounts of slightly stronger heating (enhancement of 0.2 K day^{-1}) at 850 hPa for the NEP and NA. The CSH and SLH meanwhile have stronger heating at 500 hPa for the NEP (enhancements of 2.4 K day^{-1} and 1.3 K day^{-1}) and NA (enhancements of 0.8 K day^{-1} and 0.4 K day^{-1}). As seen in the MERRA-2 wave-specific profile averages, MERRA-2 has more of a bimodal distribution with peaks at low and mid-levels, while the observed wave-specific profiles tended to show a pronounced mid-level maximum (Fig. 1.8). It is worth noting that while the domain mean values from Table 1.1 might seem weaker than expected based on results from the wave-specific profile averages (Fig. 1.8), they are a result of accumulating and averaging the heating within 500 km of the kinematic center rather than directly from the wave center as done for the previous profiles. These results show clear differences in the magnitude and vertical

structure of heating occurring around the kinematic center and directly at the kinematic center. Based on results from Hollis and Martin (2021) that examined the precipitation within a 500 km radius of the TEW center, the heaviest rainfall may not occur directly at or near the TEW center, but further outside.

Ultimately, we find that there are significant contributions of latent heating to the global background from TEWs. Figs. 1.13-1.15 show the percent contribution from the conditional (wave-specific) average latent heating rates (Figs. 1.10-1.12) to the unconditional (background) latent heating rates (Figs. 1.2-1.4) for each dataset. The percent contributions were calculated using the average latent heating rates of TEWs corresponding to orbital matches (Fig. 1.12-1.15) divided by the background heating (Fig. 1.2-1.4). This fraction was then multiplied by a frequency weight that was calculated by dividing the total number of non-missing grid points within 500 km of the TEW kinematic center by the total number of times there was non-missing data at each grid point (i.e., regardless of the presence of TEWs). Unlike with the TRMM/GPM data, the background for MERRA-2 is derived from all available times since there is no missing data. Consequently, the conditional heating rate was first multiplied by the TEW frequency of occurrence (i.e., number of TEWs divided by total MERRA-2 3-hourly times) before calculating the resultant percent contribution.

While there is moderate disagreement in the magnitude of latent heating between CSH and SLH in the conditional and unconditional 2D composites, there is generally more agreement in the percent contributions with SLH showing slightly stronger global mean contributions at both vertical levels. Table 1.1 provides the domain mean percent contributions for the NEP and NA. While stronger conditional average TEW heating occurs in the NEP relative to the NA, TEWs generally appear to contribute slightly more latent heat (i.e., higher percentage) in the NA

(e.g., 7.5% and 6.3% for the NEP and NA at 500 hPa in CSH, respectively). Due to the stronger conditional latent heating at 500 hPa (Figs. 1.10-1.12), the percent contributions are also greater at 500 hPa than at 850 hPa as seen in Figs. 1.13-1.15 and in the domain means in Table 1.1. As previously cautioned about the relatively weak domain mean heating rates in Table 1.1, it is important to also note that the percent contributions are higher when focusing on smaller areas within the subdomains, where there are larger numbers of TEW occurrences.

The percent contributions from TEWs for MERRA-2 (Fig. 1.15 and Table 1.1) show significantly higher contributions than those of the observed heating (Figs. 1.13-1.14). While the distribution of maximum contributions somewhat matches that of the CSH and SLH (e.g., large contributions over West Africa and the NA, and higher contributions at 500 hPa), the overall amount of latent heat found to contribute to the global background is much higher in MERRA-2. For example, at 850- and 500 hPa in the NA, MERRA-2 contributions range from 10-40% with smaller areas showing contributions of 50% or higher within the NA (Fig. 1.15). In contrast, both CSH (Fig. 1.13) and SLH (Fig. 1.14) show contributions in the same region closer to 10-30%. Since MERRA-2 has consistently overestimated the strength of diabatic heating, it is not unexpected that it would also show higher percent contributions than when compared to the observed data. However, it is important to consider that while the MERRA-2 conditional latent heating accumulations were matched to the corresponding times of non-missing CSH occurrences, there is inherently more heating to accumulate within the 500 km of the wave center in MERRA-2 due to the spatially continuous nature of reanalysis data (i.e., orbital data is confined to the swath widths and only fill part of the averaging domain). The previous explains the presence of additional noise in the CSH and SLH percent contributions. It thus remains possible that a spatially continuous record of observed orbital data might contain percent

contributions closer to those found in MERRA-2 due to reduced noise or additional sampling of waves not accounted for with the satellite products.

1.4. Summary and Conclusion

This study created a 17-year global climatology of diabatic heating associated with TEWs using satellite orbital and reanalysis data. Specifically, we used the TRMM version 6 CSH and SLH observed heating estimates and the MERRA-2 temperature tendency data. We first established the unconditional background diabatic heating, with special emphasis on four high TEW track density domains. The main results are limited to the Northeast Pacific (NEP) and North Atlantic (NA) domains where most waves occur at 850 hPa. Similar analysis is reproduced for the Southeast Pacific (SEP) and South Atlantic (SA), which are provided and discussed in the supplemental chapter.

We first produced two- and three-dimensional composites of the background latent, radiative, sensible, and total heating to provide a baseline for comparative analysis of the diabatic heating associated with TEWs. The 2D composites of the observed background latent heating generally show a stronger magnitude throughout the global tropics with additional large increases in the amount of heating produced over land at 500 hPa. Similar to the observed TRMM background heating, the corresponding MERRA-2 data also shows increased convection and latent heating over land at 500 hPa. However, the MERRA-2 background latent heating generally has stronger values of heating at 850 hPa, especially over subtropical ocean areas where low-level marine stratocumulus clouds often dominate.

When examining the vertical structure of latent heating over regional domains, the low-level heating bias in MERRA-2 became more apparent, as the heating below ~ 1 km was nearly

triple the magnitude of heating at middle and upper levels. The MERRA-2 low-level maximum for the NEP was nearly 6 K day^{-1} and 3.5 K day^{-1} for the NA. Comparatively, the CSH and SLH latent heating profiles showed very weak heating below 1 km with bimodal and trimodal peaks (~2 K day^{-1} and ~1 K day^{-1}) occurring at mid-levels (~3-8 km). This discrepancy between the TRMM heating profiles and those using reanalysis data is consistent with Hagos et al. (2010) and Janiga and Thorncroft (2013) who found that reanalyses tend to overestimate the magnitude of tropical diabatic heating when compared to TRMM. Furthermore, Hagos et al. (2010) found that the TRMM heating profiles tend to exhibit maximum heating in the mid-troposphere, while reanalyses often peak in the lower-troposphere. The physical explanation for these differences is unclear, however, we suspect that one possible reason could be due to higher stratiform rain fraction in the TRMM heating estimates relative to the reanalysis heating. In addition, we speculate that the low-level heating bias found in the MERRA-2 may be related to overestimated rainfall rates from shallow marine stratocumulus clouds. It is also possible though that due to the TRMM PR's lower instrument sensitivity, the TRMM heating estimates might be more biased towards heavier rainfall that is produced by deeper convective clouds.

The observed heating showed minimal difference in the shape of the profiles between the NEP and NA, though there is some geographic variability observed in the corresponding southern hemispheric domains (see supplemental for more details). For the MERRA-2 background latent heating profiles, while the general distribution of heating is similar between the two domains, the magnitude of heating is significantly stronger in the NEP relative to the NA. These differences in the geographic variability between datasets, also hold true for the regional background radiative and sensible heating profiles. The differences in the MERRA-2 total heating profile averages for the NEP and NA backgrounds match well with differences in

the climatological vertical velocity profiles where weak positive heating in the NEP leads to weak upward motion and negative heating in the NA leads to weak subsidence.

It is well-known the latent heating term is dominate for precipitating systems and we hypothesized a similar result for TEWs. When we repeat the analysis of the regional diabatic heating profiles averages but limit the profiles only to times and locations where TEWs occur, we find dramatic increases in the magnitude of latent heating for all datasets. MERRA-2's low-level maximum more than tripled for both the NEP and NA. In additional, the wave-specific latent heating in MERRA-2 showed substantial increases in mid-level heating, likely due to increases in deep convection and stratiform rain fraction in TEWs. Since all datasets produced much stronger latent heating in the wave-specific composite profiles, the total heating also becomes strongly positive and is minimally offset by the radiative cooling (as in the case of the unconditional background profiles). Relative to the observed heating, the magnitude of the latent and total heating is more than twice as strong in MERRA-2 for the NEP. The large increase in total heating results in both regions containing strong upward motions, with the magnitude being three times stronger over the NEP. Similar to what we observed in the background heating profiles, MERRA-2 also shows much stronger heating in the NEP when limiting to only wave-specific profiles. Interestingly, the CSH and SLH also show considerably more variation between regions when looking at the wave-specific profile averages than observed in that of the unconditional background heating.

This geographic variability is more noticeable when looking at the 2D composites of latent heating rates accumulated within a 500 km distance of each TEW kinematic center. For the CSH and SLH, the broader coverage and slightly stronger magnitude of latent heating found in the NEP (relative to the NA) is more apparent at 500 hPa than at 850 hPa. When looking at the

corresponding MERRA-2 composites of wave-specific latent heating, we find much stronger heating at both vertical levels in the NEP. The overall distribution or global means for MERRA-2 show a negligible difference in the strength of heating between 500- and 850 hPa, however, there are some areas in the global tropics (e.g., over land, the Maritime continent, and west Pacific warm Pool) where there is broader coverage and stronger heating at 500 hPa. Though less obvious than observed in the MERRA-2, similar differences are observed in the CSH and SLH. We speculate that these differences observed across all datasets between the 850- and 500 hPa wave-specific latent heating are related to not only increased stratiform rain fraction found in precipitating TEWs but could also be a result of more middle- to top-heavy heating in regions that tend to produce more convective clouds. Consistent with the stronger wave-specific latent heating found at 500 hPa, the 2D composites of the percent contribution from TEWs to the unconditional background latent heating show higher contributions at 500- than 850 hPa. Rather than limiting our analysis to two vertical levels to examine the background and TEW latent heating and calculate the percent contributions, we plan to use the column integrated heating in future work. The previous will allow us to examine how the total amount of latent heating is represented in each dataset and subdomain, regardless of the large variances in the vertical distribution of heating that were identified in this work.

Finally, we find significant geographic variability in the percent contributions maps with CSH and SLH showing contributions in the NEP and NA in the range of 10-30%, while MERRA-2 shows higher contributions (although occurring in more isolated regions) of 30-70%. While the MERRA-2 domain mean contributions in the NEP and NA are somewhat similar, there are notable differences in the distribution of heating found in the 2D composites. The NEP shows smaller percent contributions that cover a larger area relative to the higher contributions

found in the NA. We surmise that this could be a result of less intense rainfall from more stratiform type clouds in the NEP whereas the NA may produce more intense pockets of rainfall from clouds that are more of the convective type. This geographic variability is much less pronounced in the CSH and SLH. It is important to consider that while MERRA-2 has consistently shown stronger diabatic heating and larger percent contributions, its unlimited grid of non-missing data allows for more accumulation of latent heating in the 2D composites compared to the orbital heating data.

Regardless, and despite the unavoidable limitations of using the CSH and SLH orbital latent heating, we find that there are significant contributions of latent heating in northern hemispheric domains where TEWs occur most frequently for all datasets. The southern hemispheric domains show a trivial amount of contribution of TEW latent heating, due to not only the lower density of TEW tracks (Fig. 1.1), but in the case of the TRMM data especially, the general lack of latent heating data in those particular subtropical domains. The lack of heating data in these regions is likely to be a result of the TRMM PR's weakened sensitivity to lighter rainfall that is more common to the SEP and SA subdomains. At the time of this study, the TRMM version 6 heating product record ends before incorporating GPM precipitation data that has higher instrument sensitivity and better detects light rainfall. In the future, we plan to utilize the newer TRMM/GPM heating products to minimize biases that exclude weaker precipitating clouds.

In addition, future work will include quantifying differences in precipitation characteristics across the TEW lifecycle and delving further into identifying sources of wave-to-wave variability and seasonality (the latter are preliminarily discussed in the supplemental analysis). We also plan to repeat our analysis using the TEW tracks identified at 700 hPa, since it

has been shown that there are more occurrences of TEWs in the southern hemisphere for the 700 hPa TEW database (Hollis and Martin 2021). Preliminary work showing some differences between the two databases has already been achieved and is described in the supplemental section. Further supplemental work includes reproducing the results in the main body of this thesis for the southern hemispheric domains.

TEW Latent Heating Domain Means							
	Conditional Average (K day^{-1})			Percent Contributions (%)			Level
	Global	NEP	NA	Global	NEP	NA	
CSH	2.3	2.4	2.3	1.6	4.6	4.9	850 hPa
	4.1	4.8	3.1	2.4	6.4	7.4	500 hPa
SLH	1.4	1.7	1.6	2.2	4.9	4.4	850 hPa
	2.4	3.0	2.0	2.8	6.3	7.5	500 hPa
MER	2.5	3.7	2.5	3.2	9.5	9.0	850 hPa
	2.7	3.5	2.3	5.7	14.3	17.3	500 hPa

Table 1.1. Spatial averages of global, NEP, and NA conditional average latent heating rates and domain percent contributions for 1998-2015. Domain averages were calculated by excluding grid points with a value of zero and neglecting missing data.

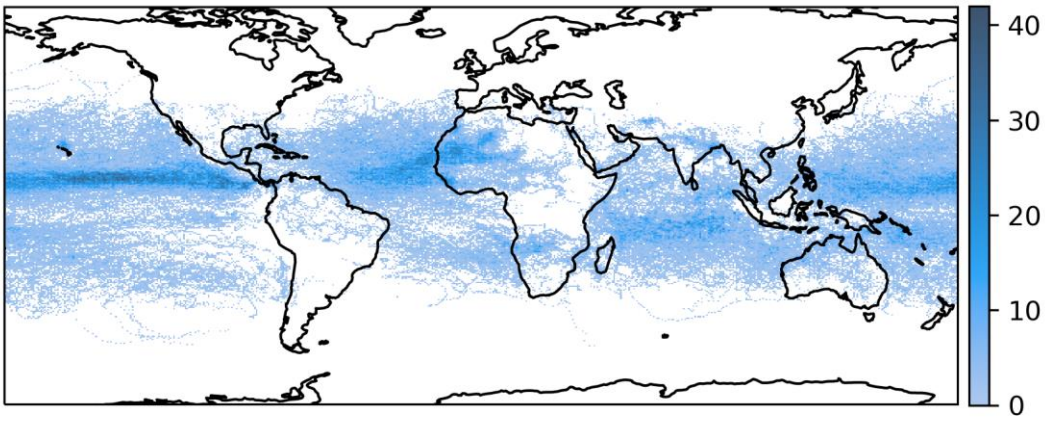

FIG. 1.1. TEW track number of occurrences at 850 hPa for 1998-2015 after filtering out TCs identified by IBTrACKS. The tracks are similar to the full climatology in Hollis and Martin (2021), although only shown for the period overlapping the TRMM/GPM heating used in this study.

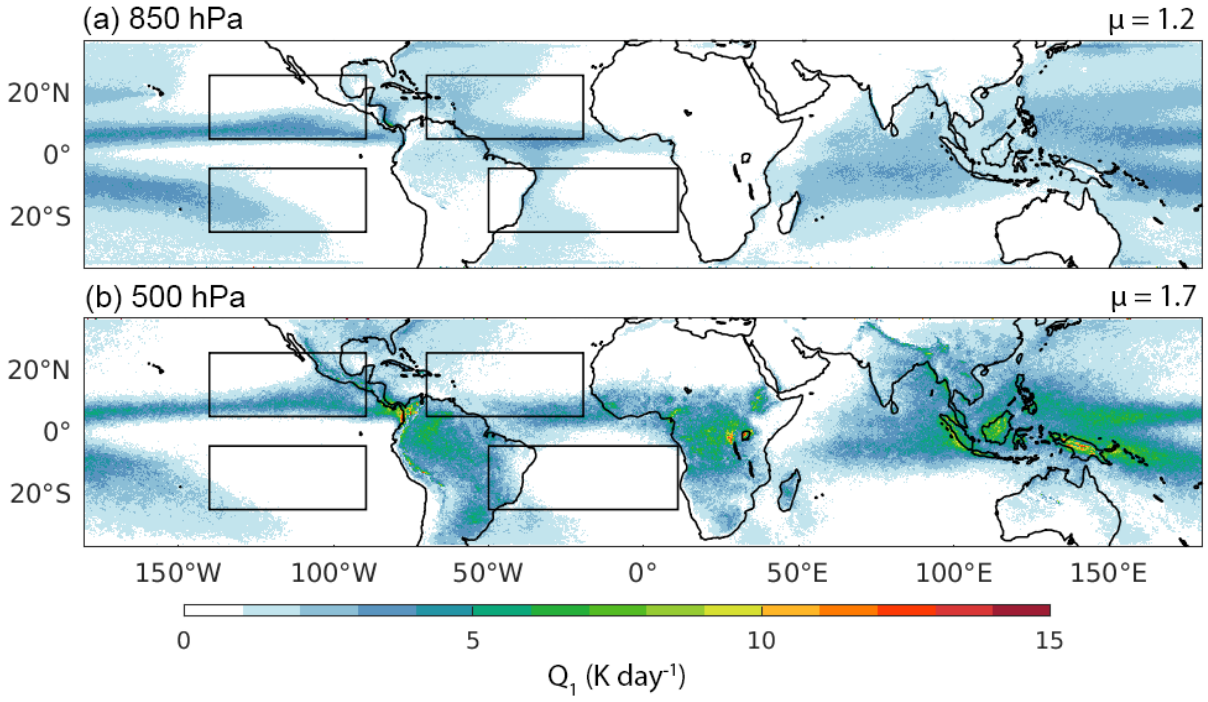

FIG. 1.2. Unconditional (i.e., background) average latent heating rates at (a) 850 and (b) 500 hPa for CSH from 1998-2015. The global mean (μ) at the top-right of each panel lists the spatial average of conditional latent heating rates, filtering out grid points with a value of zero or missing data. The black boxes represent the subdomains used in this study, including the Northeast Pacific (NEP), North Atlantic (NA), Southeast Pacific (SEP), and South Atlantic (SA).

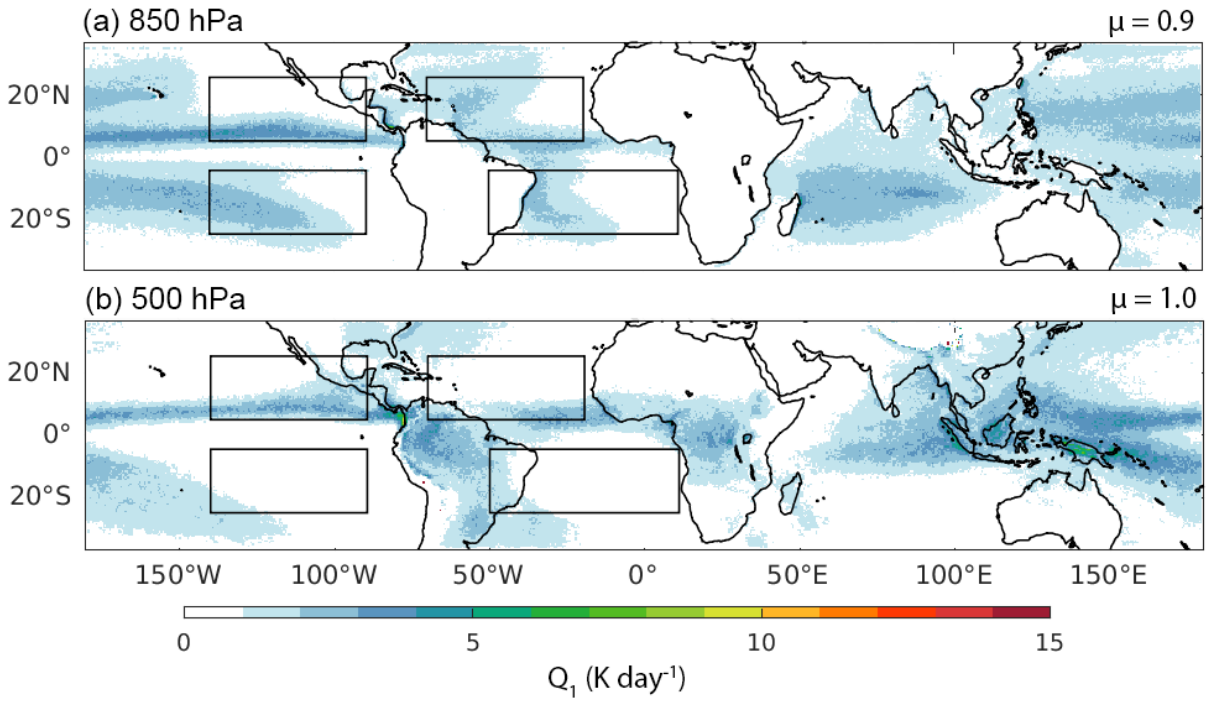

FIG. 1.3. As in Fig. 1.2, but for SLH.

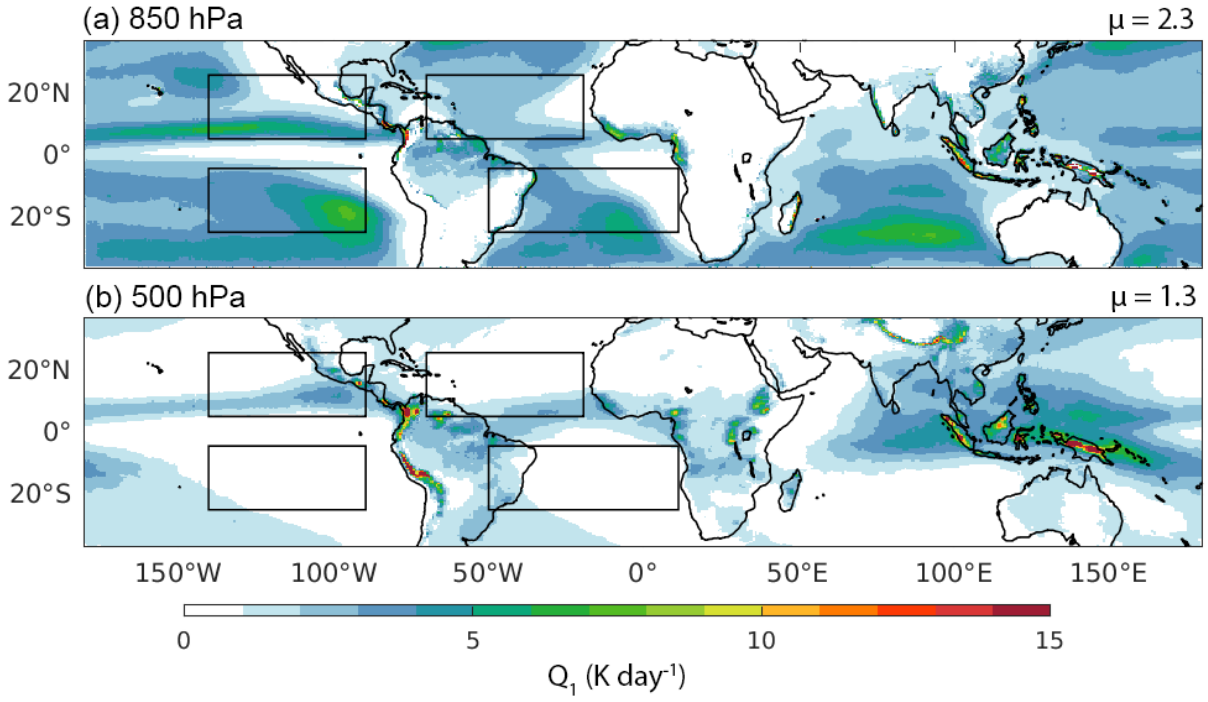

Fig. 1.4. As in Fig. 1.2, but for MERRA-2.

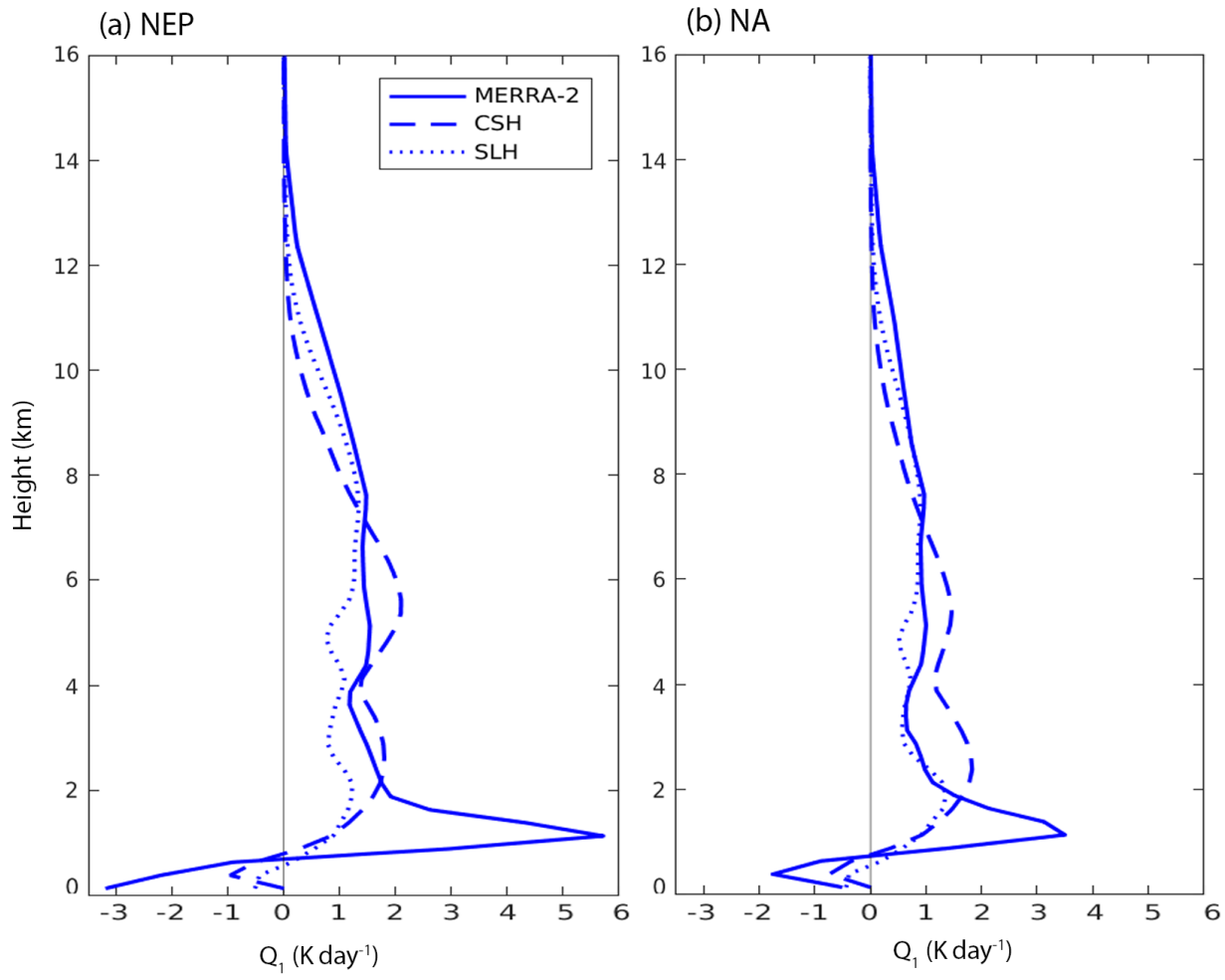

FIG. 1.5. Spatially averaged, background (1998-2015) latent heating profiles from each dataset for the (a) NEP and (b) NA using the subdomains defined in Fig. 1.2. All data use the same vertical resolution (0.25 km) where the MERRA-2 pressure grid was transformed and interpolated to match the observations.

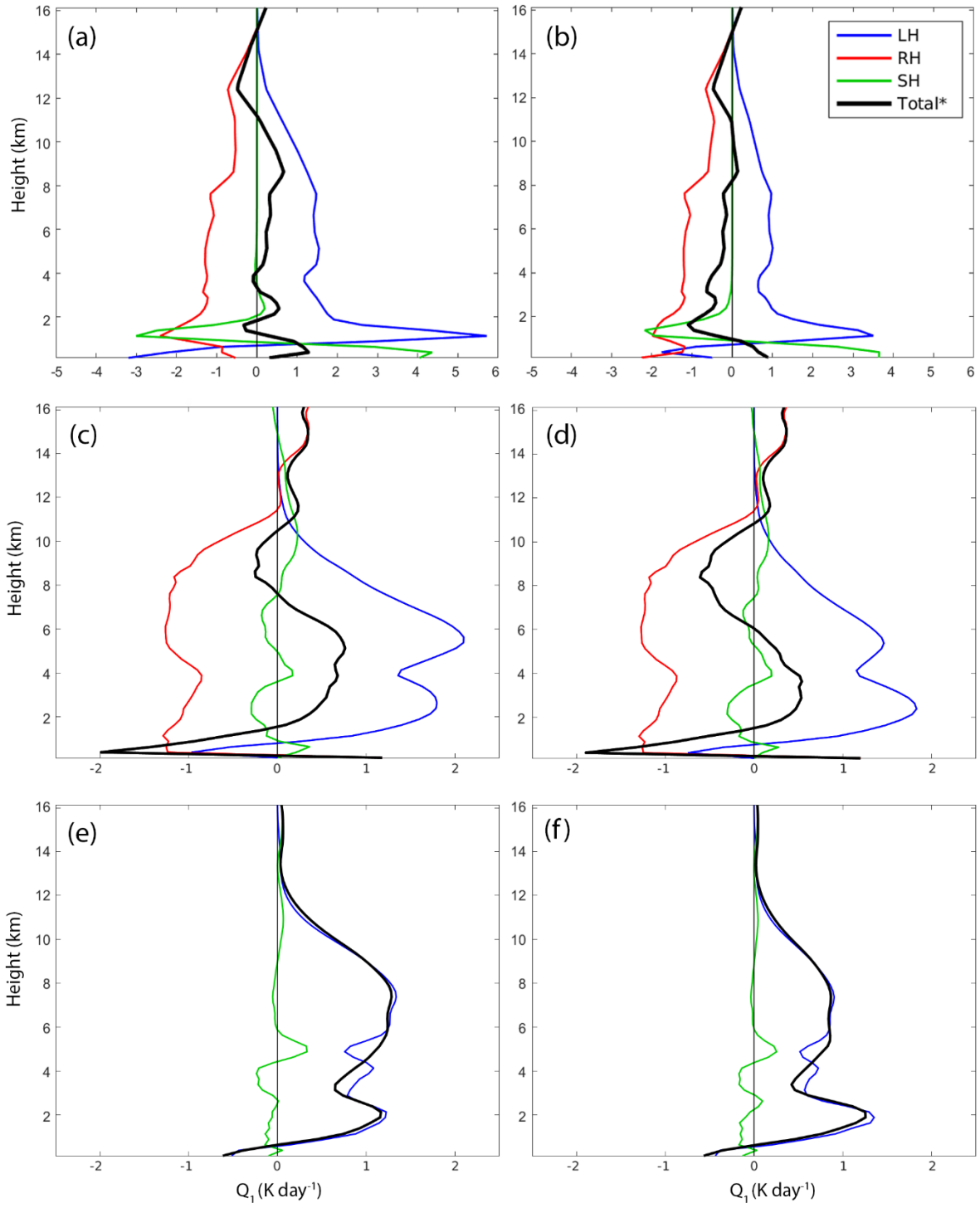

FIG. 1.6. As in Fig. 1.5, but for each diabatic subterm including latent (blue), radiative (red), and sensible (green) heating. The total (black) heating is shown for each dataset. Regional domain averages for the (a, c, e) NEP and (b, d, f) NA are shown in the left and right columns, respectively.

The (a, b) MERRA-2, (c, d) CSH, and (e, f) SLH are shown in separate rows. The MERRA-2 panels have a different abscissa due to large differences in the magnitude of heating. The SLH does not have a radiative subterm and the total heating (i.e., Q_1 – RH) should not be directly compared to the total heating (i.e., LH+RH+SLH) for MERRA-2 and CSH.

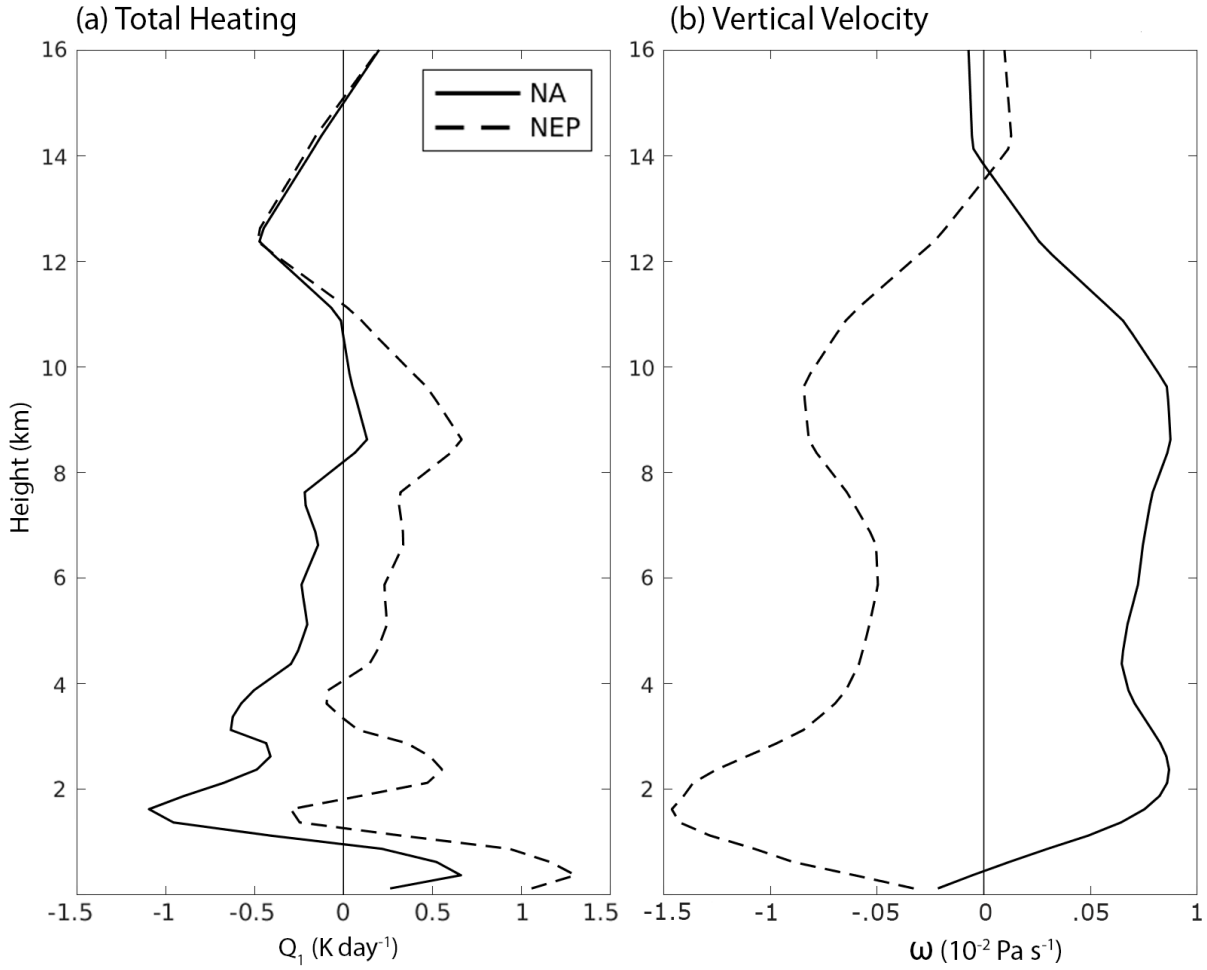

FIG. 1.7. MERRA-2 regional average profiles of background (1998-2015) (a) total heating and (b) pressure vertical velocity. The lines represent the NEP (dashed) and NA (solid) domain averages.

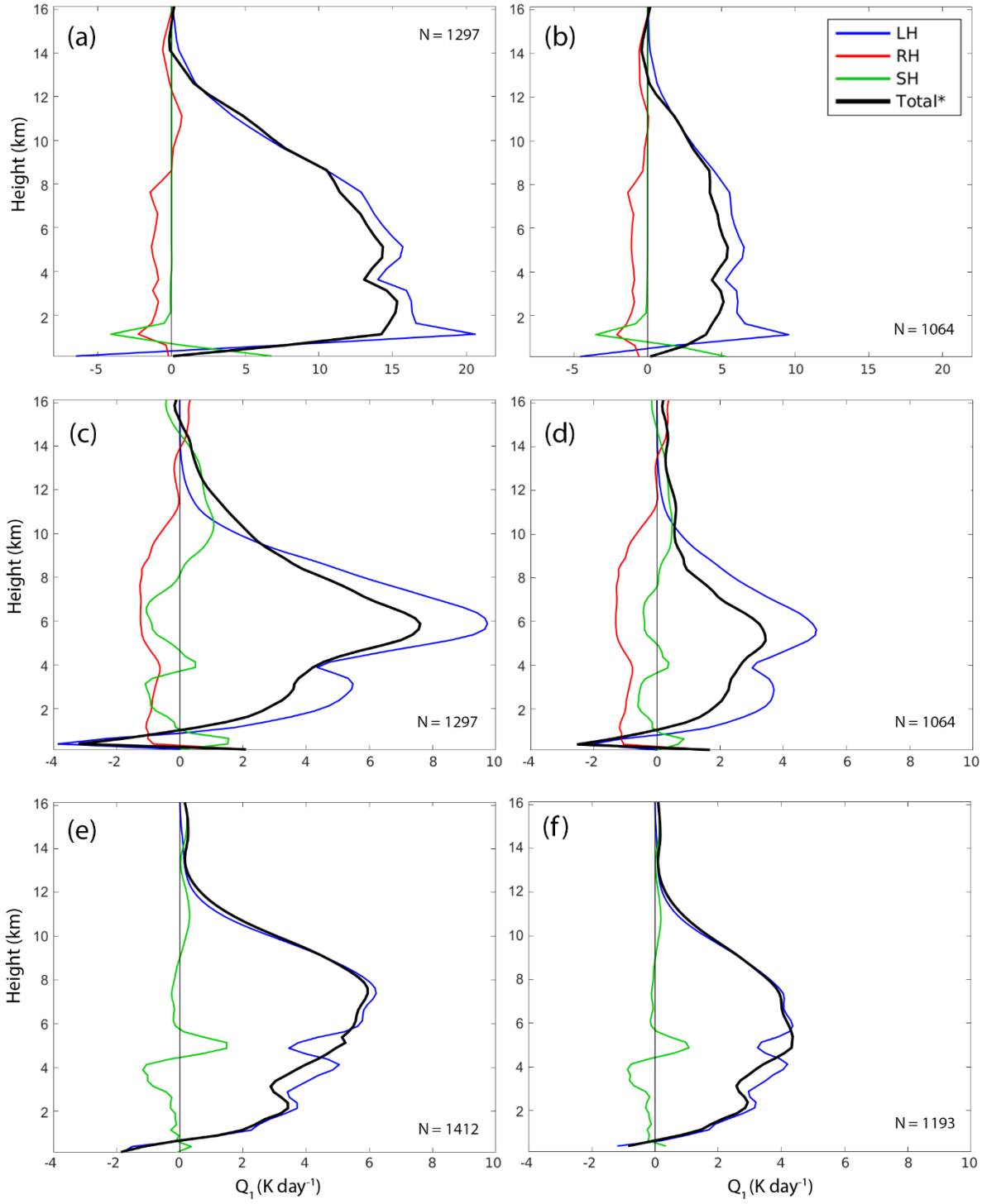

FIG. 1.8. As in Fig. 1.6, but for averages taken from the kinematic center of TEWs (i.e., "wave-specific" or conditional heating profiles). The number of samples (*N*) given in the upper-right or lower-right indicate the number of TEW tracks occurring within each subdomain that correspond

to non-missing orbital data. The MERRA-2 profiles are only composited when matching to non-missing CSH data (see text for further details). The abscissa for the MERRA-2 data varies due to the presence of stronger heating in that dataset.

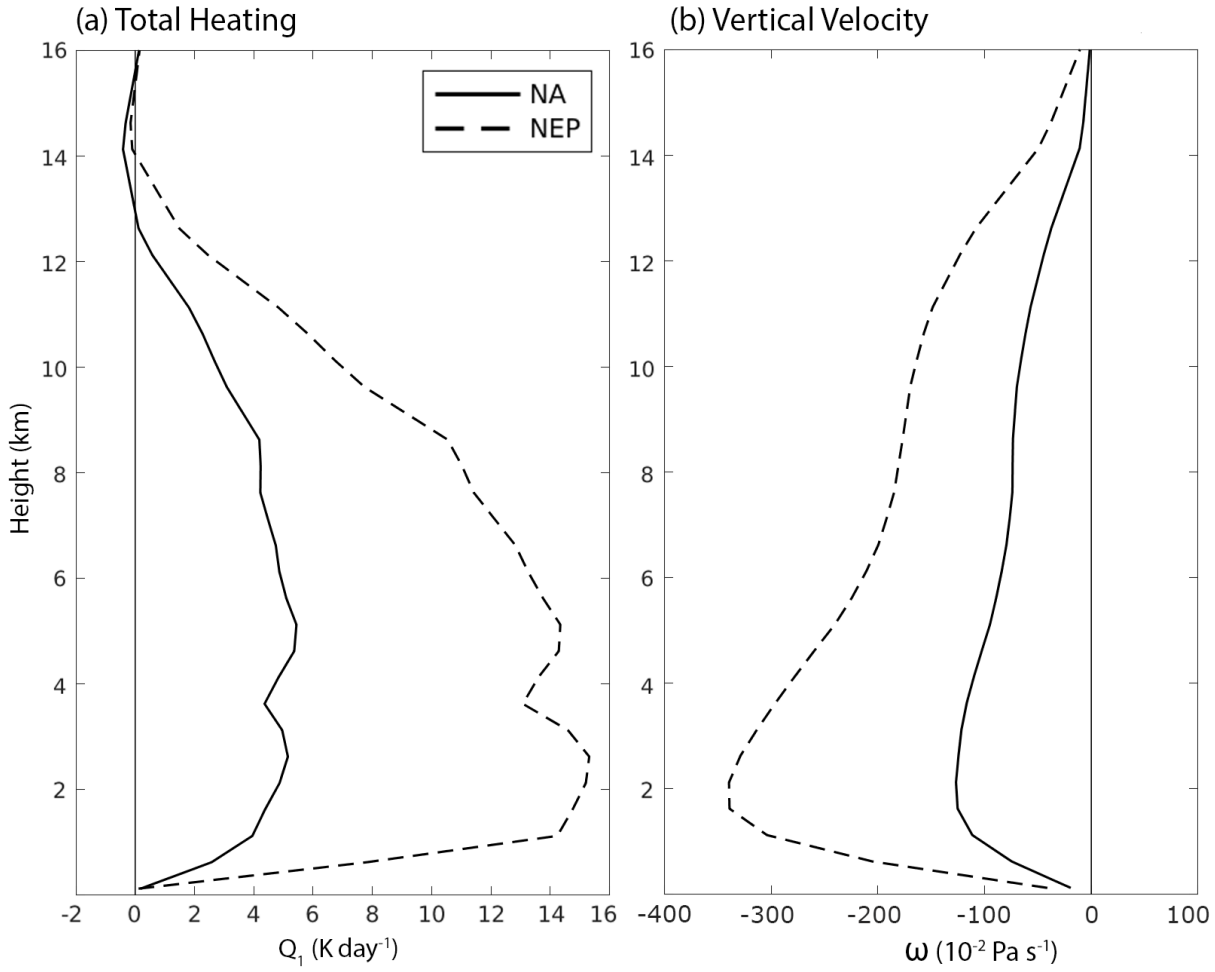

FIG. 1.9. As in Fig. 1.7, but for the regional profile averages taken from the kinematic center of TEWs for MERRA-2.

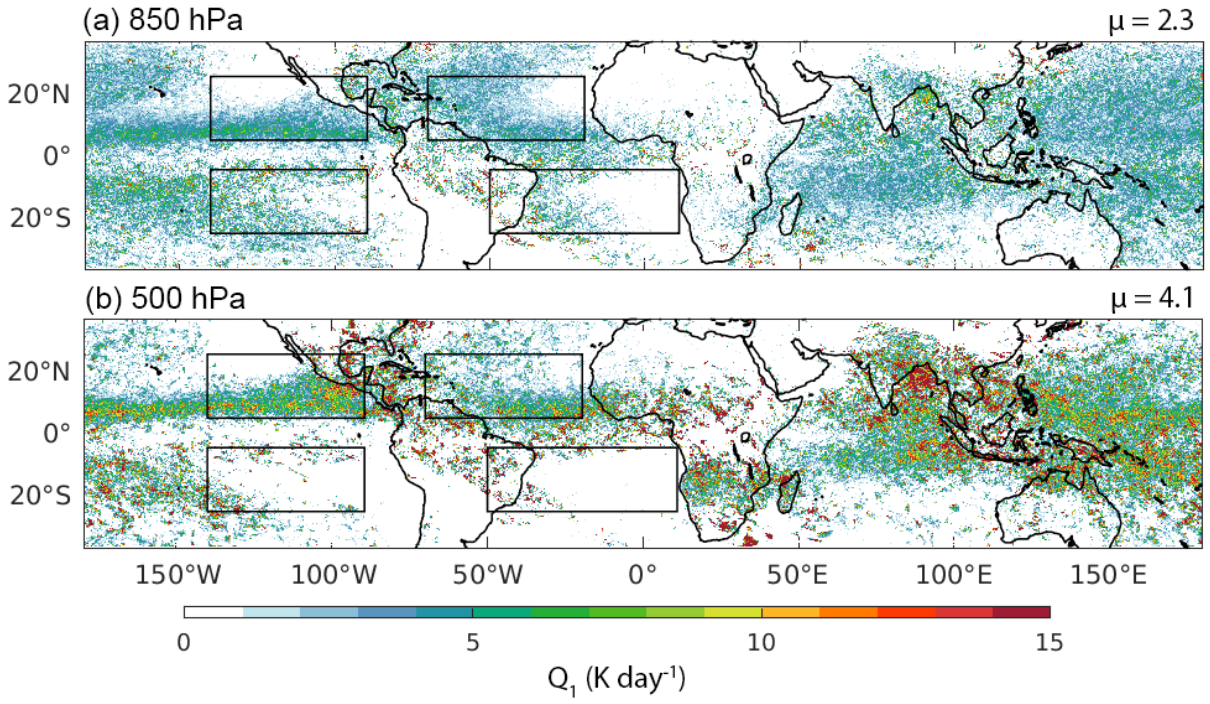

FIG. 1.10. Conditional (i.e., wave-specific) average latent heating rates accumulated within 500-km of the TEW kinematic center at (a) 850 hPa and (b) 500 hPa for 1998-2015 using CSH data. As with Fig. 1.2, the global means (μ) are listed in the upper-right of each panel. Locations where TEWs do not occur are plotted as zero heating.

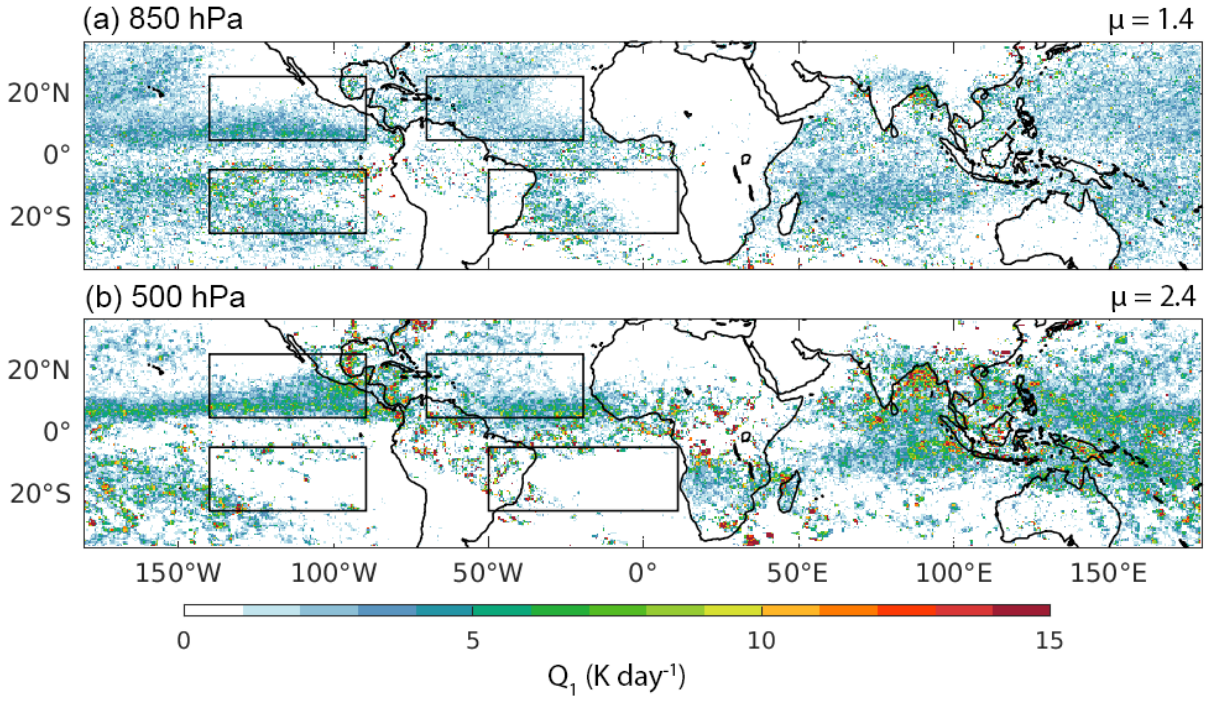

FIG. 1.11. As in Fig. 1.10, but for SLH.

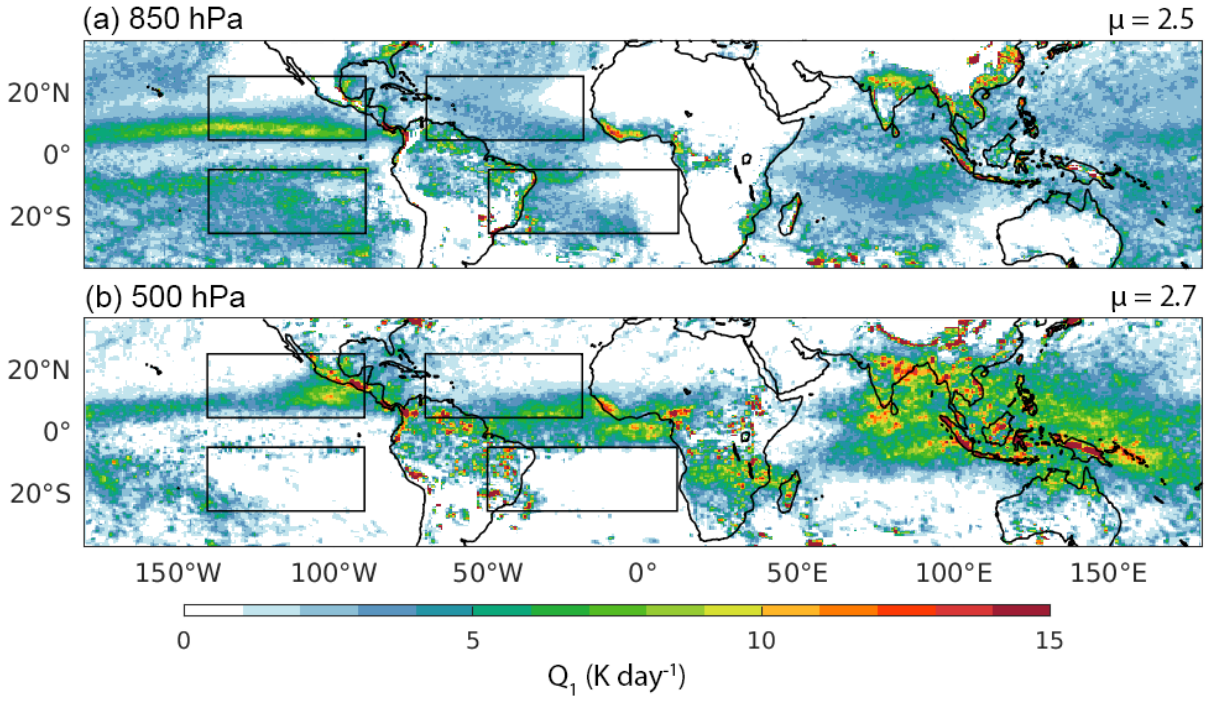

FIG. 1.12. As in Fig. 1.10, but for MERRA-2 latent heating. The composites were created using only TEW tracks that correspond to the times and locations of successful coincidences with CSH data.

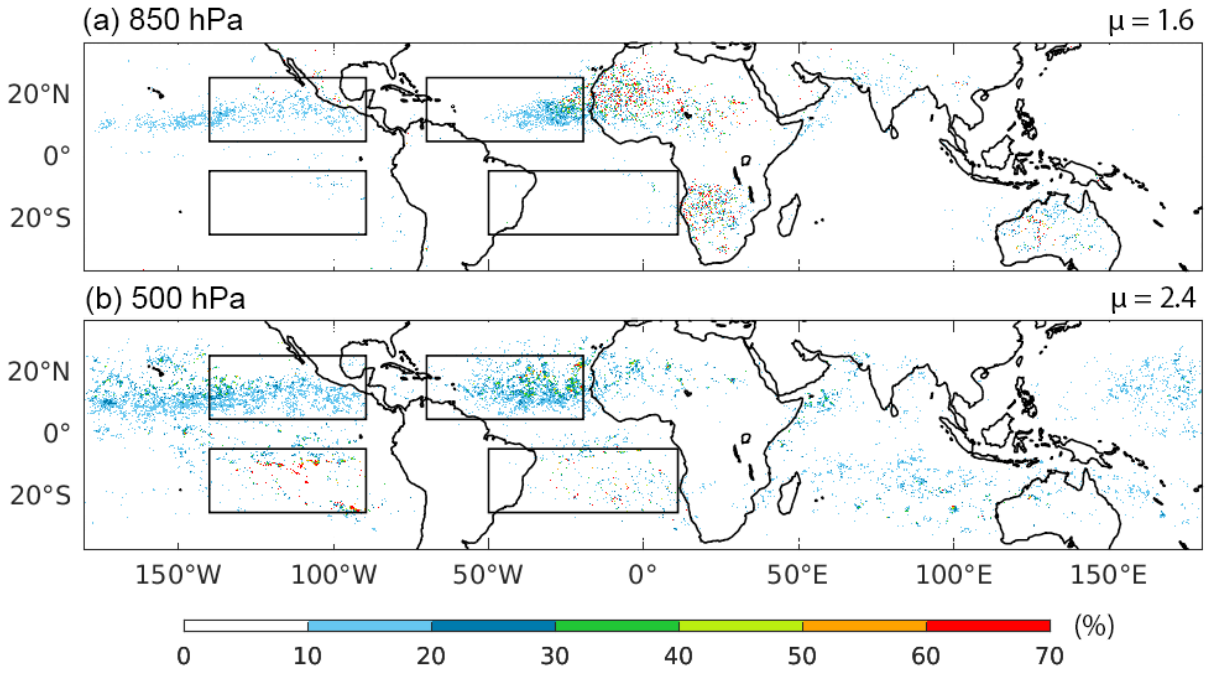

FIG. 1.13. Percent contribution of latent heating accumulated within 500 km of the TEW kinematic centers (i.e., wave-specific or conditional, Fig. 1.10) to the climatological (i.e., background or unconditional, Fig. 2) heating for the CSH. The percent contribution is shown for (a) 850 hPa and (b) 500 hPa. Global means (μ) are shown in the top-right of each panel.

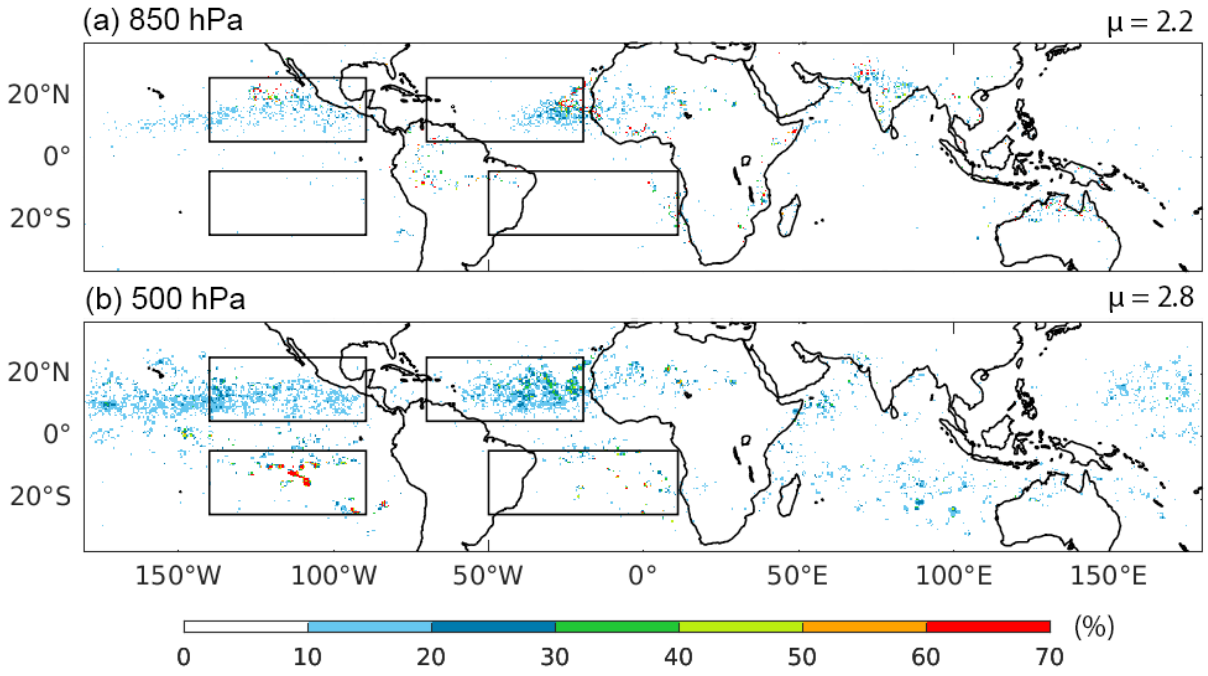

FIG. 1.14. As in Fig. 1.13, but for SLH.

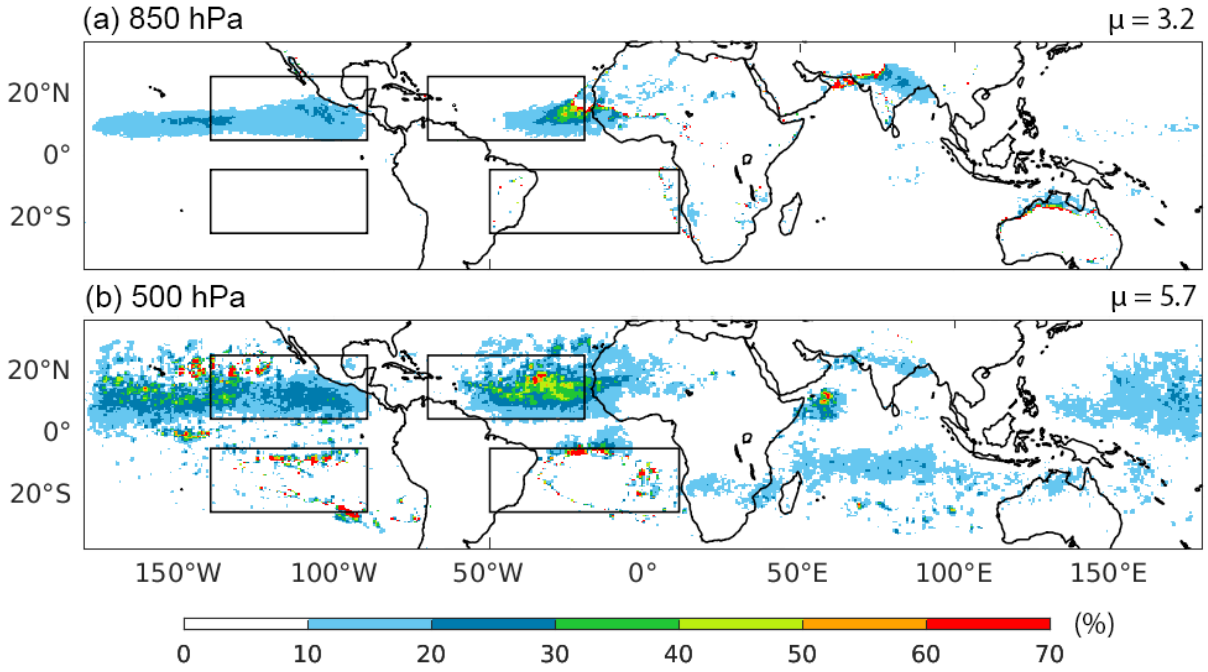

FIG. 1.15. As in Fig. 1.13 but for MERRA-2.

Chapter II: Supplemental Analysis

2.1. MERRA-2 Data and Interpolation

The NA regional annual average profiles of all terms for 1998 are shown in Fig. 2.1. The MERRA-2 heating contains three dominant terms that are most physically similar to those from TRMM including the tendency of air temperature due to moist processes (DTDTMST), radiation (DTDTRAD), and turbulence (DTDTTRB). Following Yanai et al. (1973) and to compare to the available terms from the TRMM heating data, we classify and interpret the above as LH, RH, and SH, respectively. Similar to the CSH described in the previous section, the total apparent heat source (TOT) is defined as the summation of each of the previous terms (LH + RH + SH) so that the physical processes represented in the reanalysis total more closely match the satellite observations. We note that the original total heating from reanalysis (DTDTANA) is comprised of additional processes not represented in the TRMM heating, including temperature tendencies due to friction, dynamics, physics, and gravity wave damping. In addition to these physical processes, the MERRA-2 total is also comprised of a non-physical adjustment term to account for the assimilated temperature observations. Since the previous physical and non-physical processes are not represented in the TRMM heating our modified total for MERRA-2 is more appropriate for comparison to the TRMM data.

To facilitate comparison of MERRA-2 to the TRMM observations, we transform the vertical grid through a linear interpolation scheme that uses MERRA-2 edge heights or mid-level geopotential heights. To evaluate the reliability of the interpolation scheme, latent heating profiles were plotted in Fig. 2.2 over individual land and oceanic grid points for January 1998. Two vertical resolutions were tested (250 and 500 m) in the interpolation scheme and are

compared to the original data using the “asm” mid-level heights. Fig. 2.2 shows nearly identical vertical profiles before and after interpolation for both land and ocean, with a slight (generally < 10%) underestimation of latent heating at lower levels where the maximum is reached. The interpolation otherwise demonstrates reliability throughout the rest of the vertical levels. Since there is minimal difference in the 250 and 500 m vertical spacing, we used the latter as it is less computationally demanding to regrid, process, and store the 3-hourly MERRA-2 data.

2.2. Southern Hemispheric Domain Analysis

Fig. 2.3 shows the unconditional (i.e., background) average diabatic heating profiles for the Southeast Pacific (SEP; left panels) and South Atlantic (SA; right panels) for each dataset. There are significant differences between Fig. 2.6 and Fig. 1.6, which presented the climatology for northern hemisphere domains. One major variation in the southern hemispheric background profiles is the lack of mid-level latent heating across all datasets. For MERRA-2, there is minimal latent heating above 2 km, although it is nearly twice as strong in the SA than in the SEP (Figs. 2.6a-b). At lower levels, the MERRA-2 latent heating shows a higher magnitude of latent heating in the SEP relative to the SA. This strong low-level heating bias in both domains is consistent with results from the northern hemispheric domains in Chapter 1. Latent heating for CSH and SLH also show much weaker magnitudes when compared to the northern hemispheric profiles in (cf. Figs 1.6 and 2.6). The observed mid-level heating is once again significantly reduced compared to the northern hemisphere although the mid-level heating in CSH and SLH still exceeds the estimates from MERRA-2. As such, the observed heating peaks occur at lower levels although about 1 km above the peaks in MERRA-2. For both MERRA-2 and CSH, the

total heating profile is clearly dominated by radiative cooling with minimal contributions from the weak latent heating, thus causing the total heating to be negative above ~1 km.

The negative total heating profiles from the SEP and SA are compared to those of the NEP and NA in Fig. 2.4. The northern hemispheric domains contain less cooling and occasional weak heating, as the case for the NEP, relative to the southern hemisphere (Fig. 2.4a). Given the strong correlation between positive total heating and upwards vertical motion (negative omega), the corresponding MERRA-2 background vertical velocity profiles unsurprisingly show mostly downwards motion with weak ascent only in the NEP (Fig. 2.4b). The SEP and SA meanwhile have the strongest subsidence, which coincides with the most negative total heating.

Similar to the conditional diabatic heating profiles for the northern hemisphere (Fig. 1.6), the SEP and SA profile averages taken from the TEW kinematic center corresponding to the times of non-missing CSH orbital data are shown in Fig. 2.5. One notable difference between the profiles is the large reduction in the number of samples (N) for the southern hemisphere using TEWs identified at 850 hPa. We thus use caution when interpreting the profiles in Fig. 2.5. The wave-specific profiles show much stronger latent heating in the SEP relative to the SA across all datasets. As expected for precipitating systems, the radiative cooling term plays only a minor role in the total heating and the latent term again dominates the total heating for the SEP. In the SA, however, the radiative cooling term still dominates the total (relative to the background profile averages in Fig. 2.3) since the latent heating term did not significantly increase (Fig. 2.5). As a result, the total heating is mostly negative in the wave-specific SA profiles, which also corresponds to the (mostly) weak subsidence seen in Fig. 2.6.

Table 2.1 provides the full geographic comparison of TEW latent heating averages and percent contributions to the background heating. Unlike the northern hemisphere, conditional

heating rates for the southern hemisphere in Table 2.1 tend to have weaker heating at 500 hPa than at 850 hPa, with the exception of the SA for CSH which indicates slightly stronger (enhancement of 0.2 K day^{-1}) at 500 hPa. The SLH and MERRA-2 southern hemispheric domains consistently show increased TEW heating at 850 hPa. For all datasets and in both hemispheres, the largest differences between low- and mid-level heating occur in the Pacific with minimal variation in the Atlantic. Consistent with the patterns observed in Fig. 1.12, the MERRA-2 heating in the SEP is drastically stronger at 850 hPa than at 500 hPa resulting in the domain mean (4.0 K day^{-1}) being nearly six times higher (Table 2.1). Consistent with the results of the kinematic center profile averages, Table 2.1 further demonstrates that MERRA-2 produces stronger heating rates at lower levels and weaker heating rates at mid-levels when compared to the TRMM heating in both hemispheres.

Given that there are only 146 and 172 samples (i.e., TEW coincidences with non-missing orbital data) in the SEP with 232 and 268 occurring in the SA for the CSH and SLH, respectively, we again use great caution when interpreting Table 2.1 for the southern hemisphere. This is especially relevant when examining the average percent contributions in the SEP and SA. Based on the larger contributions made at 500 hPa relative to 850 hPa in the southern hemisphere for all datasets (Figs. 1.13-1.15), it was expected that the domain mean percent contributions in Table 2.1 would reflect this. Instead, we find inconsistent and inconclusive results in the SEP and SA domain means. For example, while it is clear in Fig. 1.15 that there are more contributions made in the SEP at 500 hPa than at 850 hPa for MERRA-2, Table 2.1 shows an average percent contribution of 0.1% at 500 hPa and 1.2% at 850 hPa. The percent contributions in the SEP are also inclusive for the CSH as seen by the negative domain mean at 500 hPa.

The SA percent contributions are more reliable with consistency between the observed datasets and reasonable values based on the northern vs. southern hemispheric differences found in Figs. 1.13-1.15. However, MERRA-2 shows the strongest domain contribution at 500 hPa of 19.2% occurring in the SEP while the SA domain mean is only 0.1%. While there are some isolated areas of high contributions (>70%) in the SEP with mostly lower contributions (< 30%) covering a larger area in the NEP, it is still unexpected to see such a large discrepancy between the northern and southern hemispheric domain mean contributions. Aside from these SEP and SA percent contributions in MERRA-2, Table 2.1 generally shows smaller contributions of latent heating from TEWs in the southern hemisphere. The results for the SEP and SA in Table 2.1 are considered preliminary due to the small number of samples. We expect future work will be more conclusive when we repeat the analysis using the 700 hPa TEW track database that has a higher occurrence of southern hemispheric TEWs.

2.3. 700 vs. 850 hPa TEW Track Differences in Heating

Preliminary work has quantified diabatic heating variability in the TEW tracks detected at 700 hPa (Fig. 2.7) and 850 hPa (Fig. 2.8). The profiles in Figs. 2.7-2.8 are obtained by using all available MERRA-2 heating data (i.e., not limited to CSH orbital matches) for a single test year (2000). Across all four domains, the number of samples (*N*) included in the profile averages is much higher for the 700 hPa, with the greatest relative increase in track occurrences in the southern hemisphere (e.g., 786 vs. 159 TEW coincidences for the SEP at 700- and 850 hPa, respectively). There is significantly stronger heating in the waves identified at 850 hPa relative to those identified at 700 hPa (note the different abscissa), despite the higher number of occurrences at 700 hPa. That is, we find a lower number of composite profiles does not

necessarily result in weaker heating. The most striking differences in the heating magnitude occur in the Pacific domains. For example, there is weaker latent heating and more dominate cooling for 700 hPa waves due to the radiative and sensible terms for the SEP with total heating primarily negative above ~1 km (Fig. 2.7c). In comparison, the total becomes strongly positive due to the dominance of the latent heating term for 850 hPa TEWs (Fig. 2.8). This discrepancy in the number of waves vs. the strength of heating is found across each subdomain suggests that there may be a large number of non-precipitating or dry TEW features being captured in the waves identified at 700 hPa compared to those identified at 850 hPa, particularly in the southern hemisphere.

2.4. Wave-to-Wave Variability

Fig. 2.9 shows the individual mean diabatic heating terms from Fig. 2.8b (i.e., all 850 hPa waves for the year 2000 for the NA using MERRA-2) and ±1 standard deviation as calculated from all individual profiles comprising the average. For the latent heating term, the envelope of uncertainty shows a large range of roughly ±10 K day^{-1} around the low-level maximum and nearly double that found at the second mid-level peak (Fig. 2.9a). While not as dramatic, the radiative profile contains strong variations in the strength of radiative cooling found in the NA wave-specific profile averages (Fig. 2.9b). Reflective of the wave-to-wave variability found in the individual subterms, the total heating profile also shows a wide range of the strength of heating, including both negative and positive values (Fig. 2.9d).

To help understand these large variances, we construct histograms of the heating terms at 850- and 500 hPa to identify if extreme values are included in the NA profile averages (Figs. 2.10-2.11). For each term, the highest number of samples is clustered around 0 K day^{-1},

indicating the absence of clouds and precipitation, with a wider range of heating values identified at the 500 hPa level. The axes of each panel were automatically adjusted to include all representative bins and there are some extreme values, albeit a very small number, being included in the profile averages in Fig. 2.9. For the latent heating term, there appears to be a large number of extreme positive values (e.g., > 50 K day^{-1}) at both vertical levels with more extreme values occurring at 500 hPa.

2.5. Seasonal Variability

Fig. 2.12 composites the 1,732 samples in the NA for 2000 by season to identify possible sensitivities to seasonal changes in environmental conditions. The boreal winter latent heating is relatively weak (maximum value of 4 K day^{-1}), resulting in negative total heating due to more influence from the radiative cooling (Fig. 2.12a). The differences observed between boreal winter (negative total heating) and summer (strong positive total heating) in the NA are not surprising, as we expect more clear sky scenes during boreal winter due to colder SSTs limiting convection even when dynamic waves are identified from curvature vorticity. The largest number of waves in the NA occur in JJA (873) with the second largest number of TEW occurrences in SON (538). There is little variation in the radiative and sensible terms between JJA and SON, with stronger latent (and total) heating occurring in SON. The finding that TEWs occur most frequently during JJA and SON is consistent with the peak of tropical cyclones for the north Atlantic basin. Based on recent Atlantic hurricane season trends that show stronger TCs occurring in SON, it is also reassuring to see that while there is a reduction in the number of TEWs from JJA to SON, the latent heating (i.e., energy source) in TEWs is enhanced.

2.6. Analysis of Error / Performance Metrics and Inter-term Correlations

In addition to the visual dataset intercomparison provided in the composite profile averages throughout this thesis, a quantitative interpretation of MERRA-2's latent heating for the NA is summarized in Table 2.2. It is important to note that these metrics were calculated using the 3H31CSH (version 7) and 3HSLH (version 6) monthly products, which are slightly different from the revised data shown in the previous profiles. We thus acknowledge there is some limitation when comparing the metrics in Table 2.2 to the NA background profiles in Fig. 1.5. Using model performance (i.e., error) metrics such as root mean squared error (RMSE), mean squared error (MSE), and mean bias error (MBE), the vertical structure of the MERRA-2 latent heating is evaluated by comparing it to the corresponding CSH and SLH profiles. A less commonly used metric, the Hausdorff Distance (HAUS_D) is a mathematical construct to measure the closeness of two sets of points by assigning a scalar score between two trajectories and serves as a measure of shape similarity or dissimilarity. Smaller results for HAUS_D indicate improved performance by MERRA-2. Smaller values of HAUS_D also correspond with larger Pearson's correlation coefficient (PCC). Overall, the performance metrics mostly reflect what was evident from a visual analysis of Fig. 1.5.

While there is some disagreement between the performance metrics, they generally show that the vertical structure of latent heating in MERRA-2 matches that of SLH more closely than of CSH. Only one out of the seven metrics (NMSE) shows a better match between MERRA-2 and CSH. With the majority of the metrics in agreement, and a PCC value of 0.81 (compared to 0.63 for CSH), we quantitatively demonstrate that MERRA-2's prediction of latent heating more closely resembles SLH than CSH. Other interesting evaluations include confirming of a stronger similarity in SH between MERRA-2 and SLH and better performance of MERRA-2 for RH

when compared to CSH (not shown). Moreover, the statistical analysis indicated that the total heating terms contain more disagreement between MERRA-2 and CSH due to the significant differences in the vertical structure of sensible heating.

Further term intercomparison for the NA regional background heating is provided in Table 2.2. MERRA-2 and CSH were both linearly interpolated to 0 – 18 km with 0.25 km spacing to match the SLH vertical grid. Term relationships were then examined as correlations of height. Strong antisymmetry is found between latent heating and radiative heating (r = -0.89) and also between latent heating and sensible heating. Stronger correlations exist among individual terms than when compared to total heating, with the exception of the strong positive correlation between latent heating and total heating for the SLH. Consistent with previous warnings in interpreting the total heating for SLH, the only meaningful dataset intercomparison in Table 2 for SLH is between latent and sensible heating since SLH's total neglects radiative heating. Similarly, these limitations extend to SLH's correlation between sensible and total heating. The correlation of latent and total heating in MERRA-2 and CSH are both negative, although MERRA-2's is of moderate strength (r = -0.62) while CSH's is weaker (r = -0.32). These weak to moderate correlations are a result of strong radiative cooling discussed throughout Chapter 1. As expected for tropical precipitating systems, when the TEW-specific heating profiles in MERRA-2 are analyzed, the correlation between latent and total heating becomes strongly positive (r = 0.88) while the correlation for radiative cooling and total heating becomes moderately negative (r = -0.53) (not shown).

TEW Latent Heating Domain Means											
	Conditional Average (K day^{-1})					Percent Contribution (%)					Level
	GLB	NEP	NA	SEP	SA	GLB	NEP	NA	SEP	SA	
CSH	2.3	2.4	2.3	3.0	2.1	1.6	4.2	4.9	1.2	1.2	850 hPa
	4.1	4.8	3.1	1.5	2.3	2.4	5.9	7.4	-8.3	1.6	500 hPa
SLH	1.4	1.7	1.6	2.8	1.4	2.2	4.6	4.3	0.9	1.4	850 hPa
	2.4	3.0	2.0	1.0	1.1	2.8	6.0	7.5	4.0	1.6	500 hPa
MER	2.5	3.7	2.5	4.0	2.3	3.2	9.5	9.0	1.2	0.9	850 hPa
	2.7	3.5	2.3	0.7	1.3	5.7	14.3	17.3	0.1	19.2	500 hPa

Table 2.1. As in Table 1.1, but for all domain (including SEP and SA) conditional average latent heating rates and percent contributions for 1998-2015.

Error Metric	TRMM Latent Heating	
	SLH	CSH
RMSE	0.48	0.64
NMSE	0.01	0.01
MAE	0.22	0.44
MSE	0.23	0.41
MBE	0.14	-0.18
HAUS_D	3.95	5.30
PCC	0.81	0.63

Table 2.2. Performance metrics for MERRA-2's ability to represent the climatological NA background latent heating profile compared to the corresponding observed monthly TRMM product (3H31 v7 for CSH and 3HSLH v6). The metrics include root mean squared error (RMSE), normalized mean squared error (NMSE), mean absolute error (MAE), mean squared error (MSE), mean bias error (MBE), Hausdorff distance (HAUS_D), and Pearson correlation coefficient (PCC). Interpretation of the numbers (e.g., value closer to one is a more favorable comparison) is provided in the supplemental text.

Data	**Correlation Coefficient**					
	(LH, TOT)	(SH, TOT)	(RH, TOT)	(LH, RH)	(LH, SH)	(RH, SH)
CSH	-0.32	0.23	0.52	-0.89	-0.58	0.23
SLH	0.98	-0.14	-	-	-0.33	-
MERRA-2	-0.62	0.61	0.62	-0.68	-0.79	0.16

Table 2.3. Diabatic heating term intercomparison for the background latent heating profile averages for the NA using TRMM CSH (version 7) and SLH (version 6) and MERRA-2. Pearson correlation coefficients are calculated for individual term profiles (LH, SH, and RH) and TOT and between the individual term profiles (e.g., latent heating and radiative heating: LH, RH). Caution should be used when interpreting correlations for the total heating with SLH since TOT for SLH does not include radiative heating.

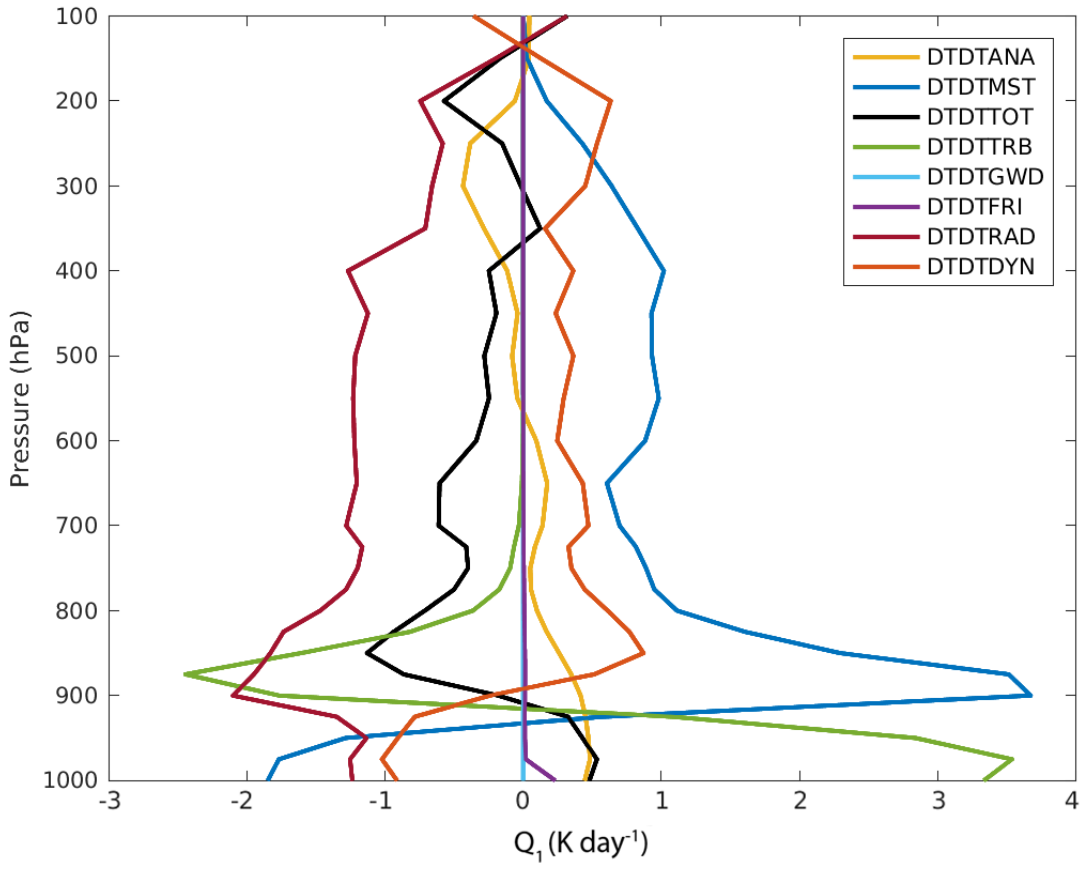

FIG 2.1. MERRA-2 NA background profile annual averages for 1998 using all available temperature tendency terms associated with the following processes: moist processes (DTDTMST), radiation (DTDTRAD), turbulence (DTDTRB), friction (DTDTFRI), dynamics (DTDTDYN), physics (DTDTTOT), and gravity wave damping (DTDTGWD). Due to the additional processes and terms, the total temperature analysis tendency term (DTDTANA) represents a different "total" heating than the MERRA-2 total heating calculated in this study (i.e., LH+RH+SH).

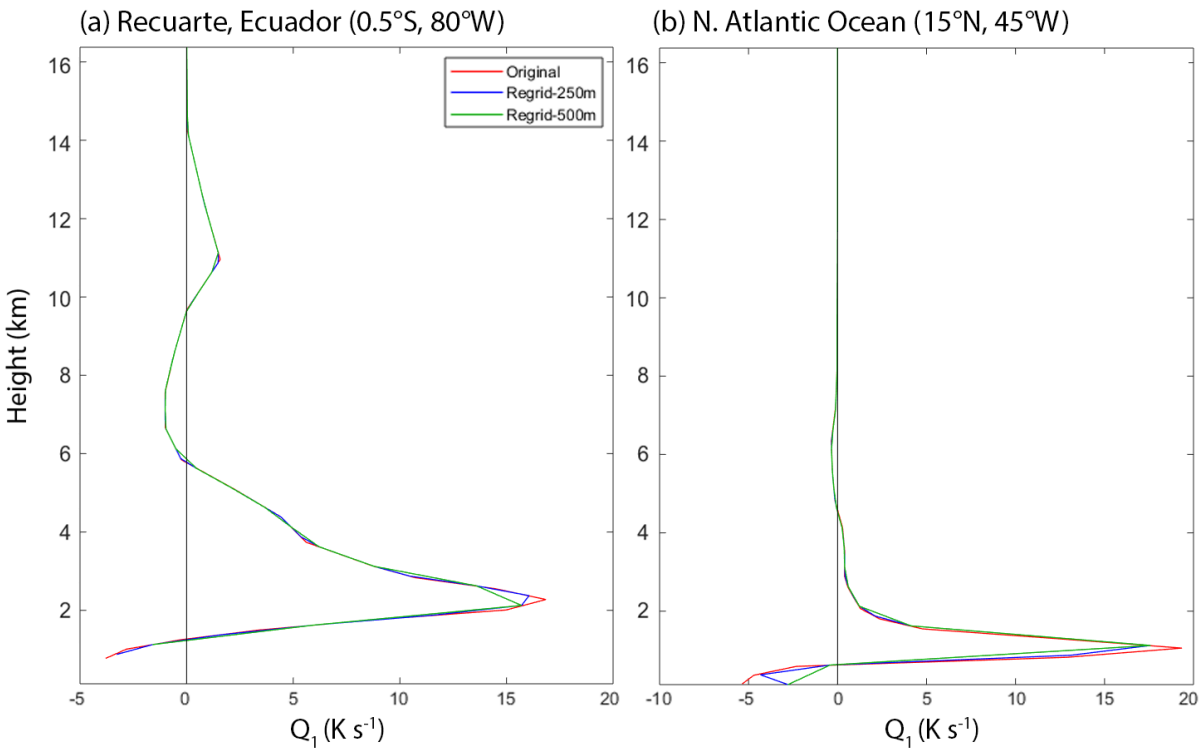

FIG 2.2. MERRA-2 latent heating profiles using the vertical cell edge geopotential height (red) and resulting profiles after interpolating from a pressure grid to a geometric grid using a 250 m (blue) and 500 m (green) vertical spacing. Profiles were created using a sample monthly test file (January 1998) for a single grid point over (a) land and (b) oceanic domains to identify potential sensitivities.

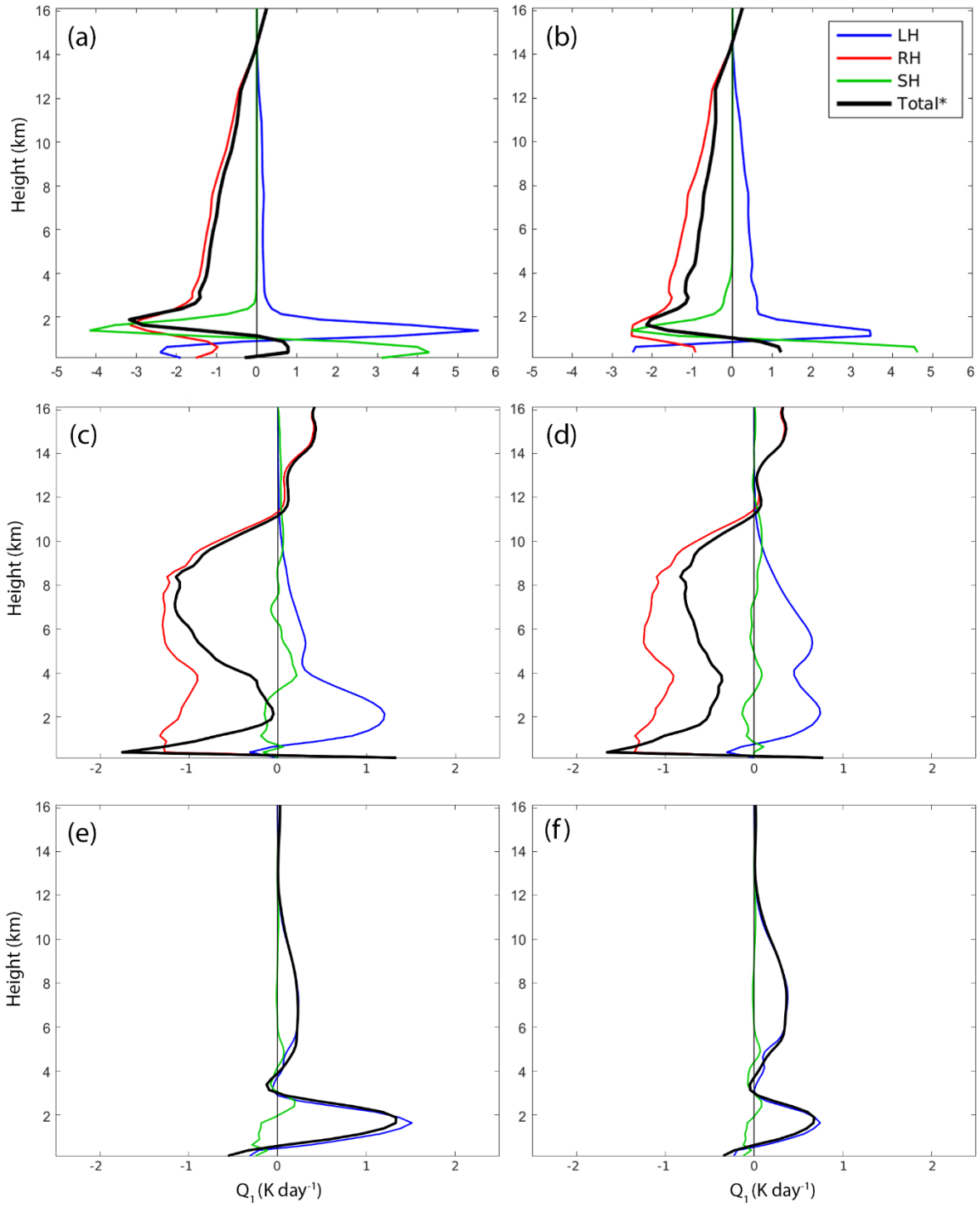

FIG. 2.3. As in Fig. 1.6, but for the (a, c, e) SEP and (b, d ,f) SA.

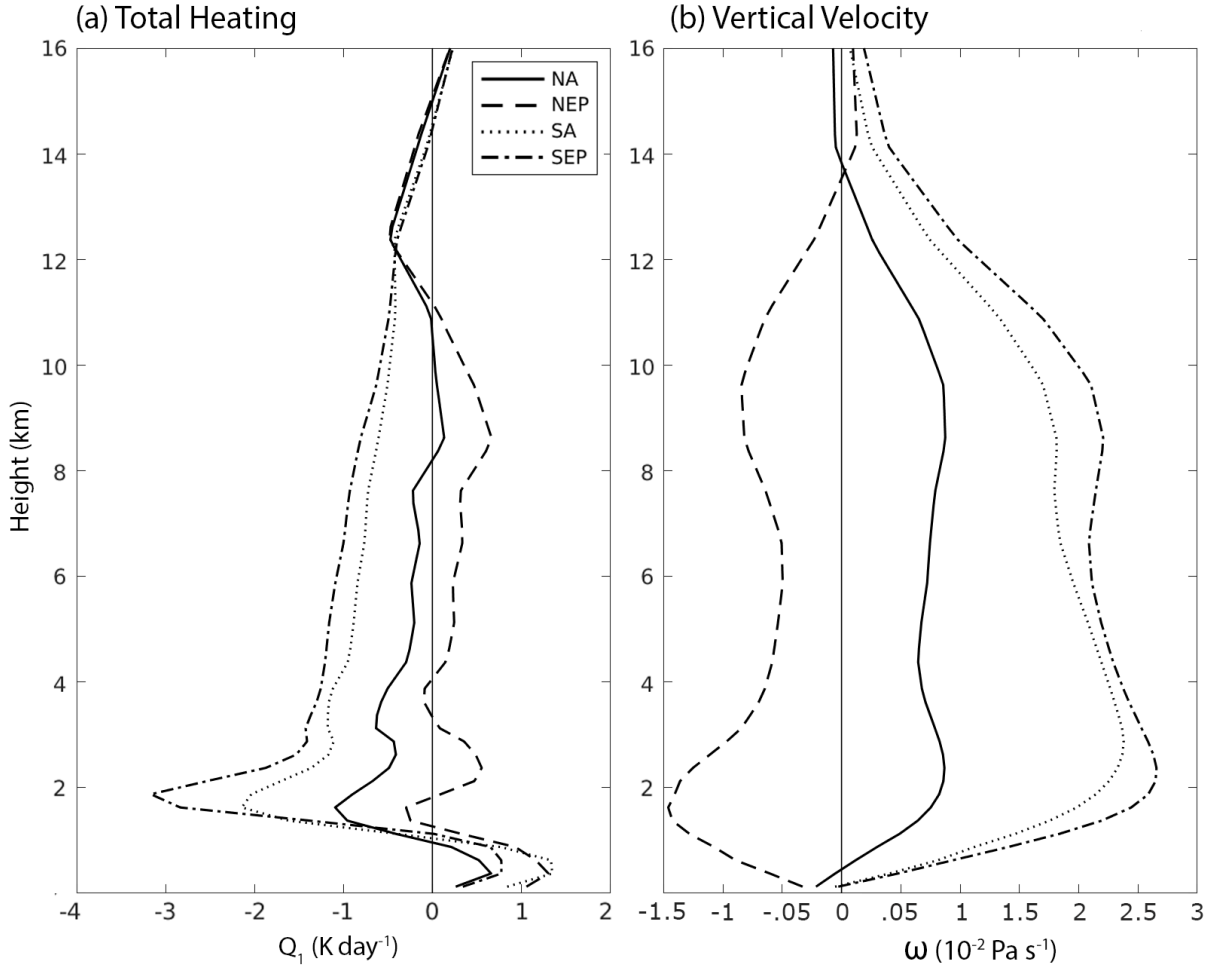

FIG. 2.4. As in Fig. 1.7, but for all domains shown in Fig. 1.2.

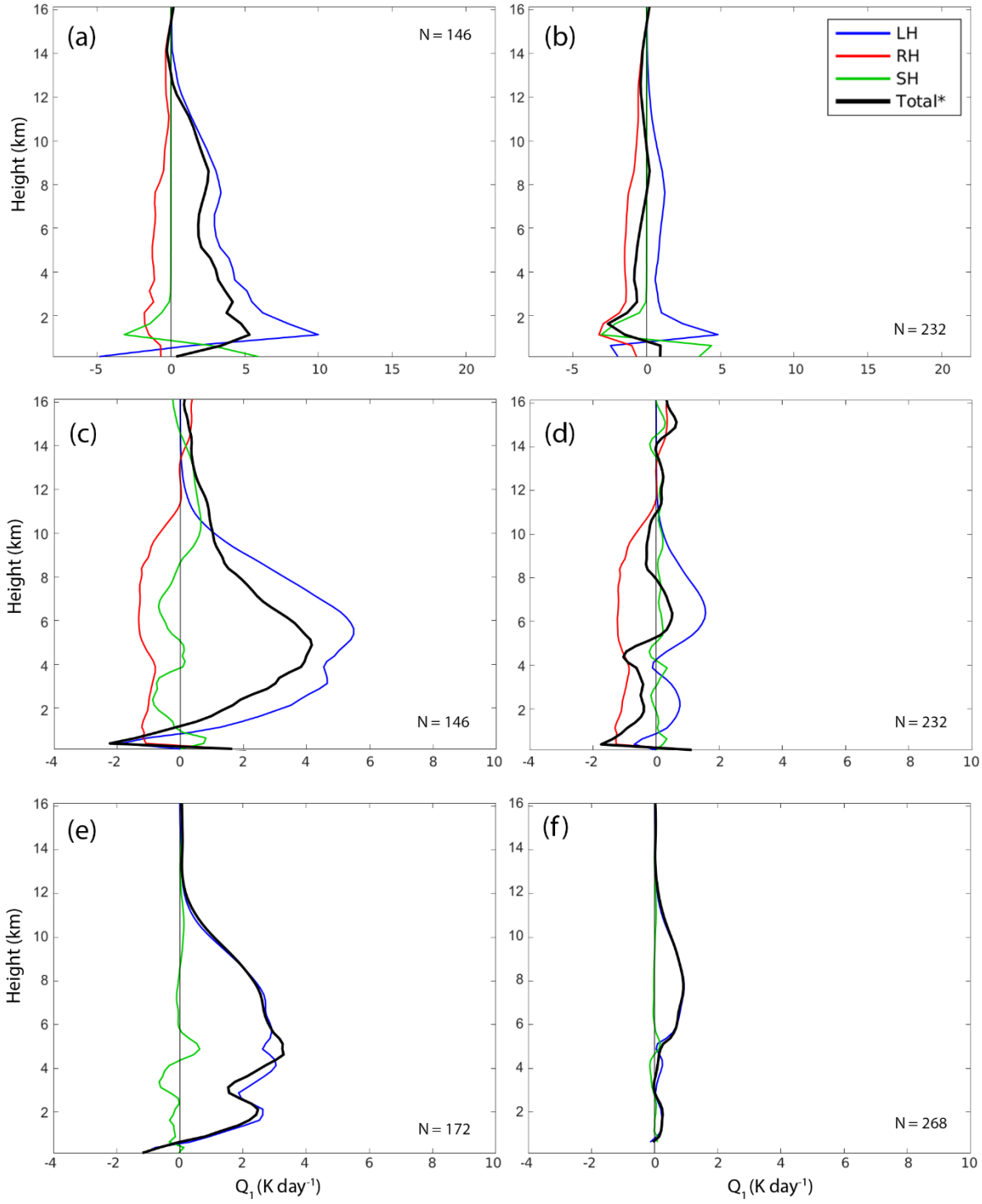

FIG 2.5. As in Fig. 1.8, but for the (a, c, e) SEP and (b, d, f) SA.

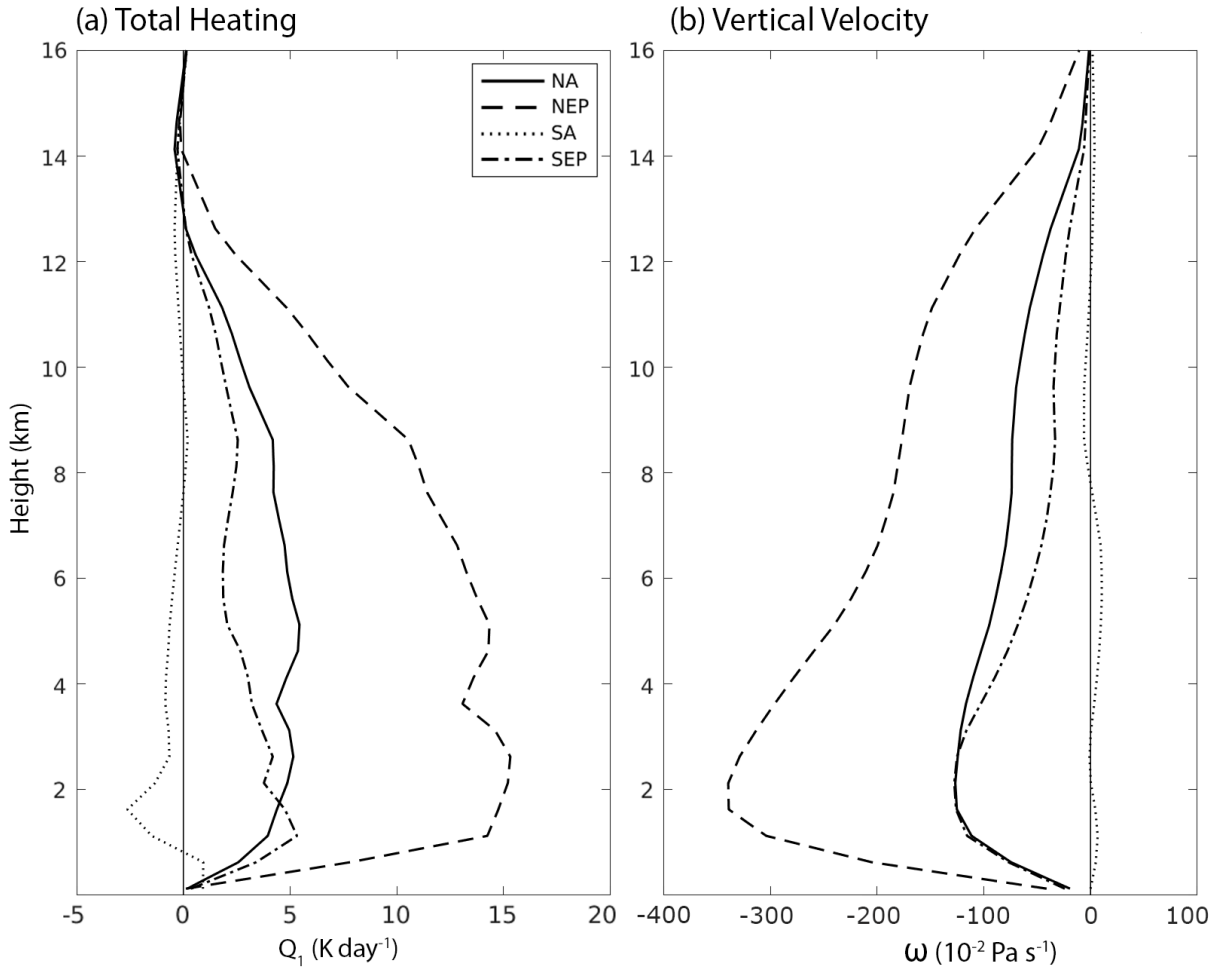

FIG. 2.6. As in Fig. 1.9, but for all domains shown in Fig. 1.2.

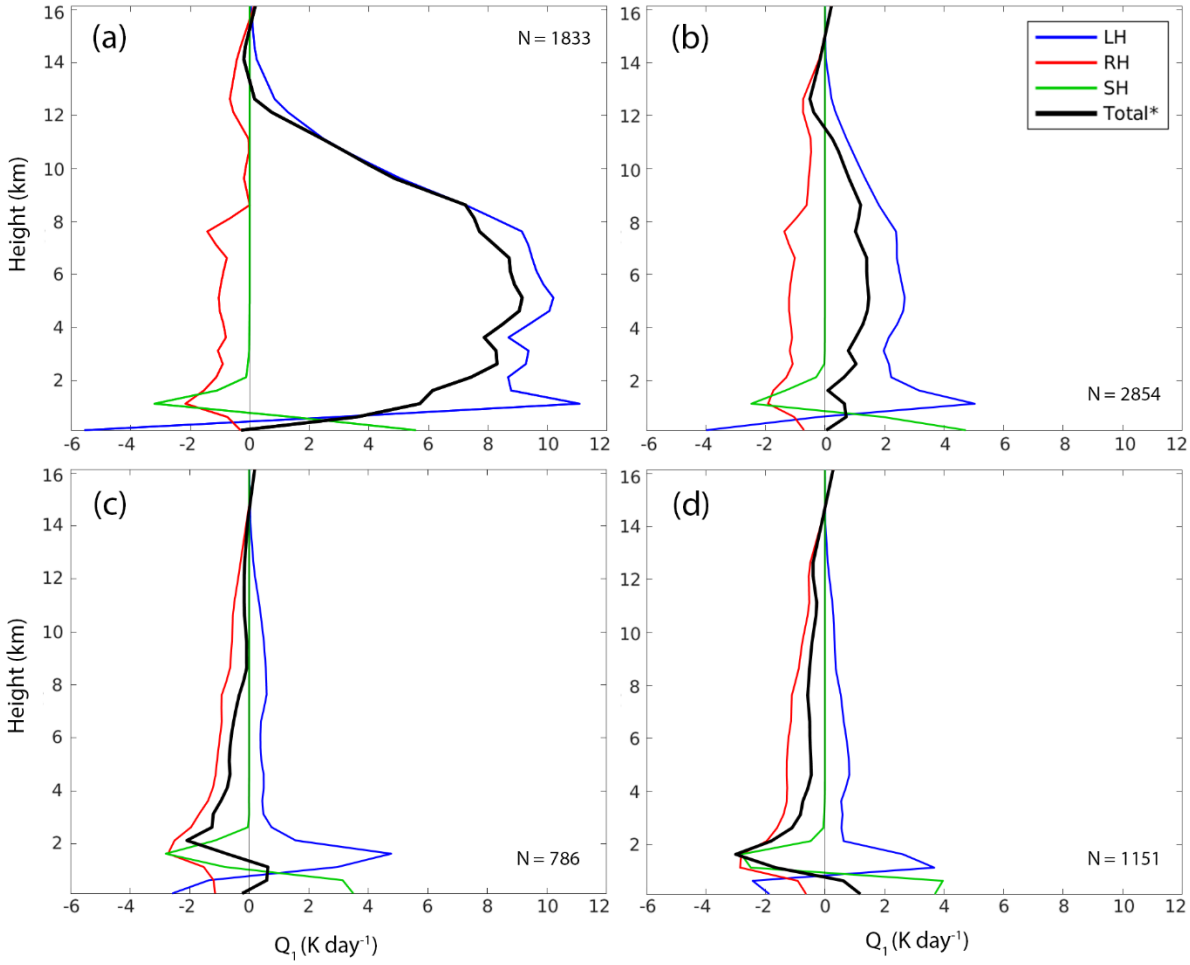

FIG. 2.7. Conditional heating profiles TEWs identified at 700 hPa for the (a) NEP, (b) NA, (c) SEP, and (d) SA. The composites use all wave data from the year 2000 and MERRA-2 heating.

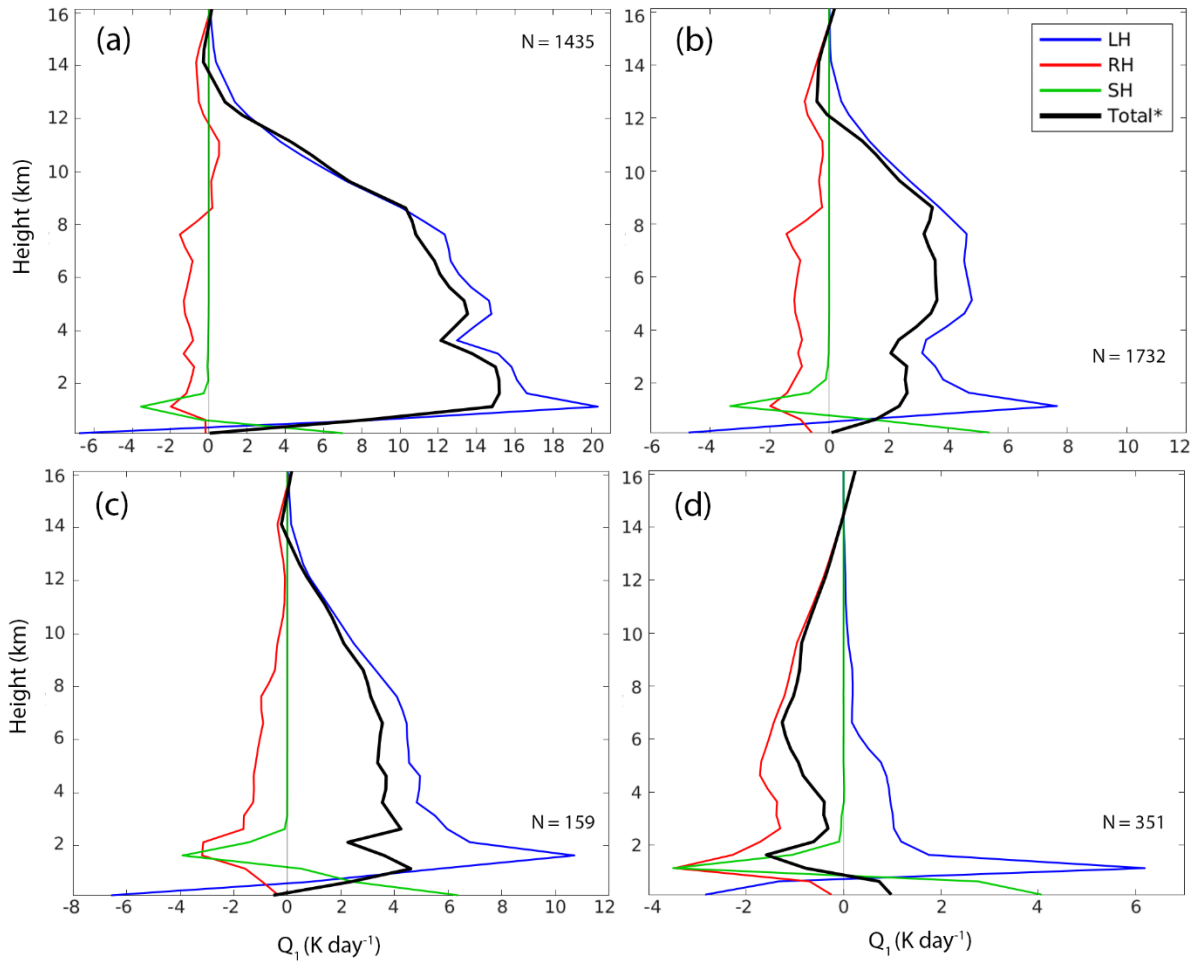

FIG. 2.8. As in Fig. 2.7, but for TEWs identified at 850 hPa.

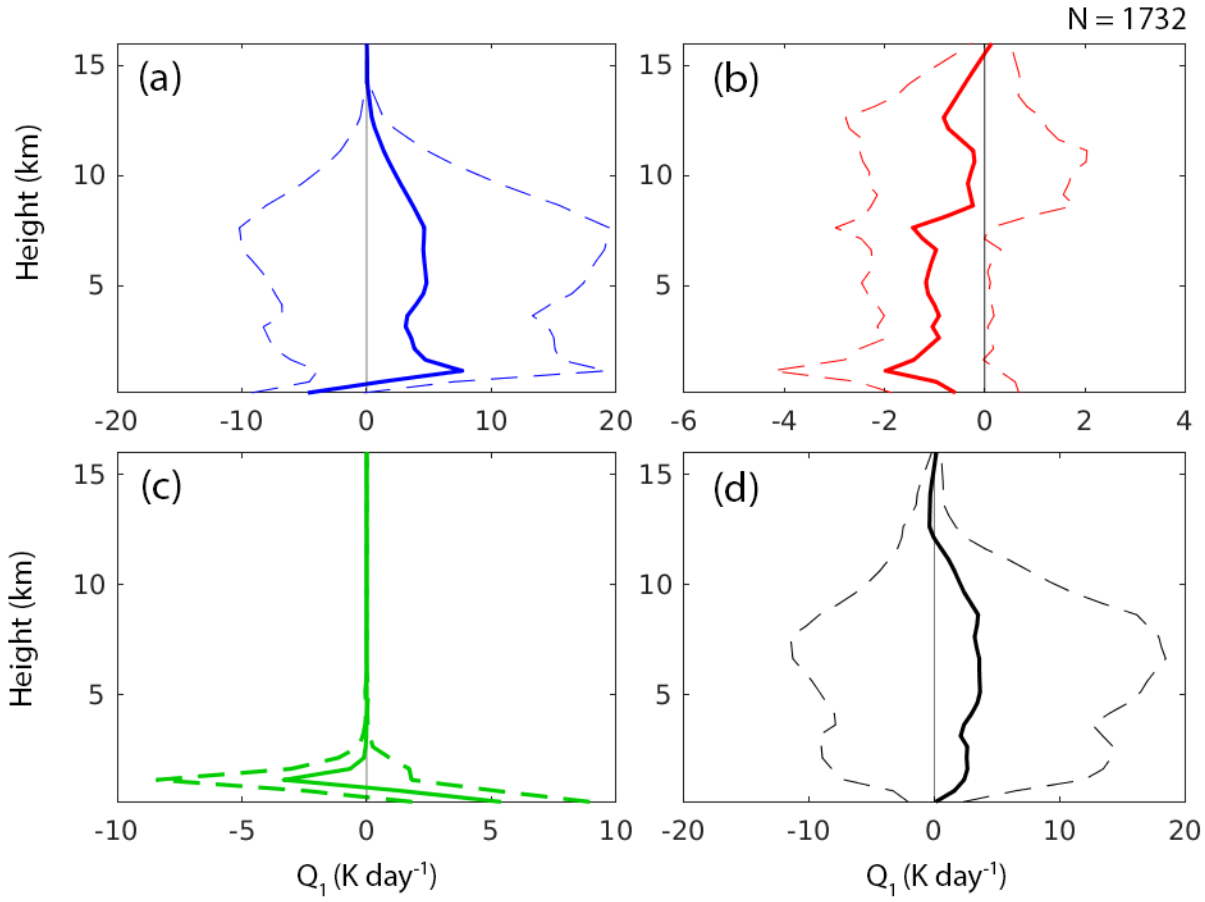

FIG. 2.9. MERRA-2 average TEW profiles (solid) and ± 1 standard deviation (dashed) for the NA using 850 hPa waves for the year 2000. The profiles include (a) latent, (b) radiative, (c) sensible, and (d) total heating.

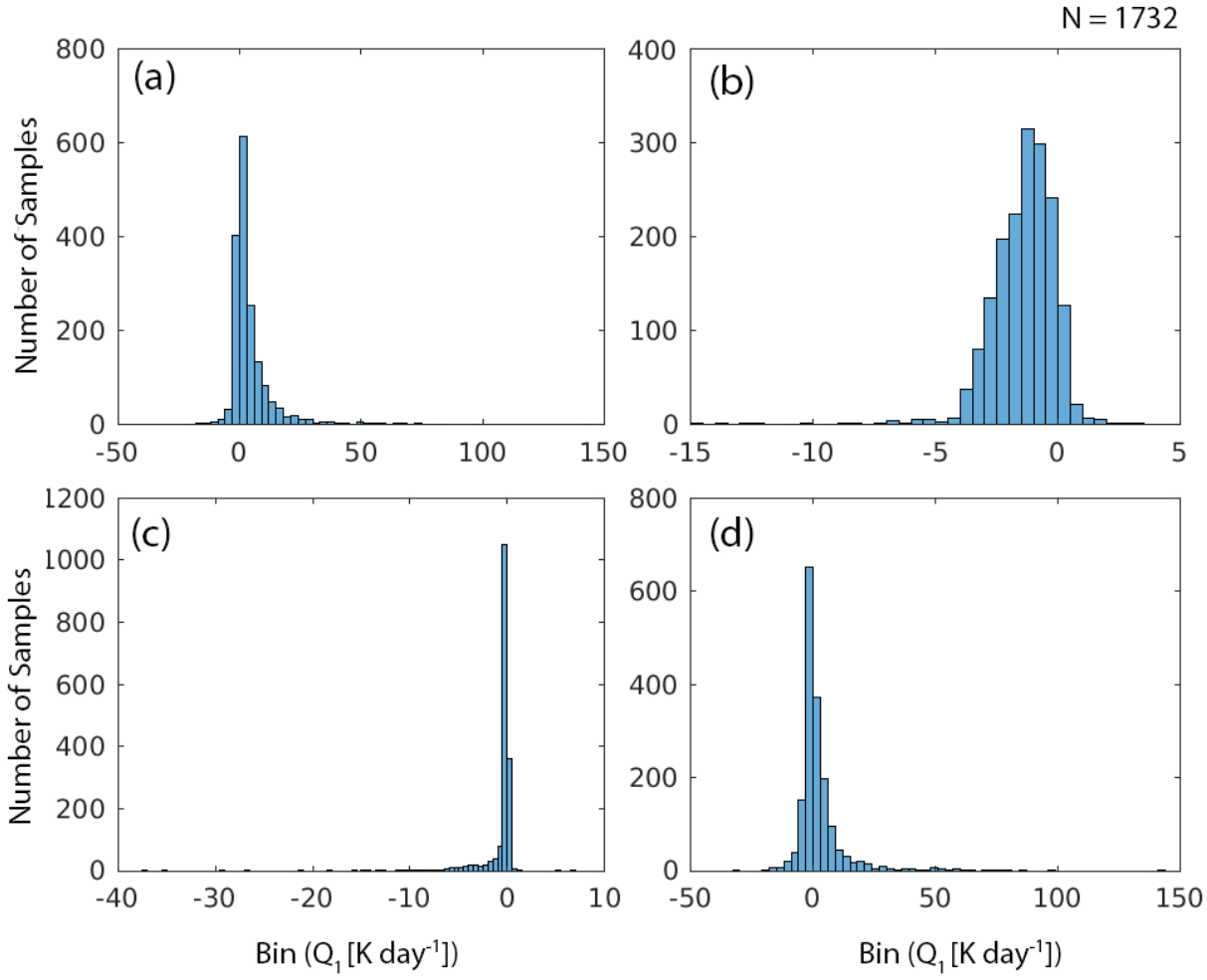

FIG. 2.10. Histograms for (a) latent, (b) radiative, (c) sensible, and (d) total heating at 850 hPa for the year 2000 using MERRA-2 heating data. All heating values are retrieved from the kinematic center of TEWs identified at 850 hPa in the NA domain.

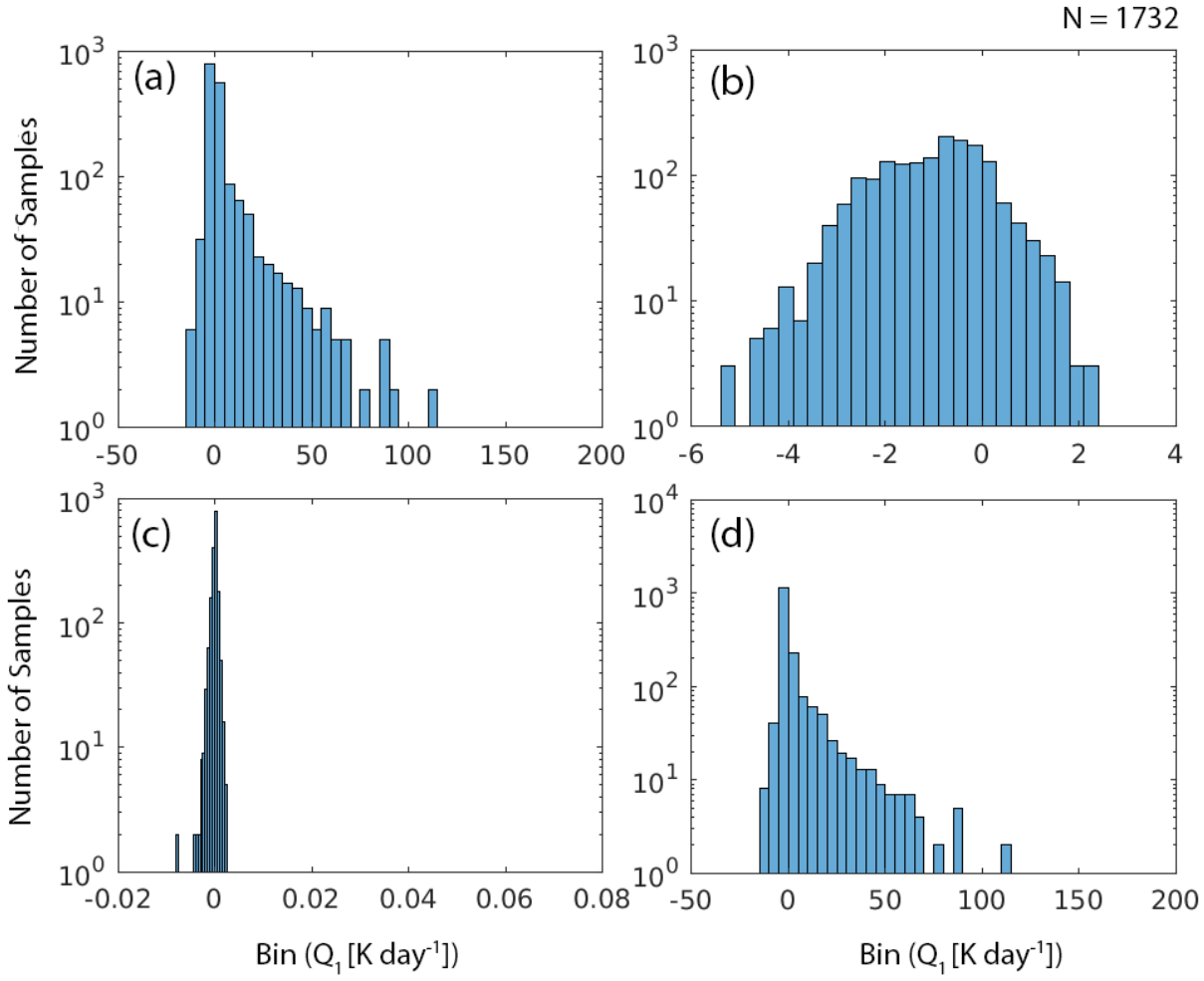

FIG. 2.11. As in Fig. 2.10, but for heating at 500 hPa.

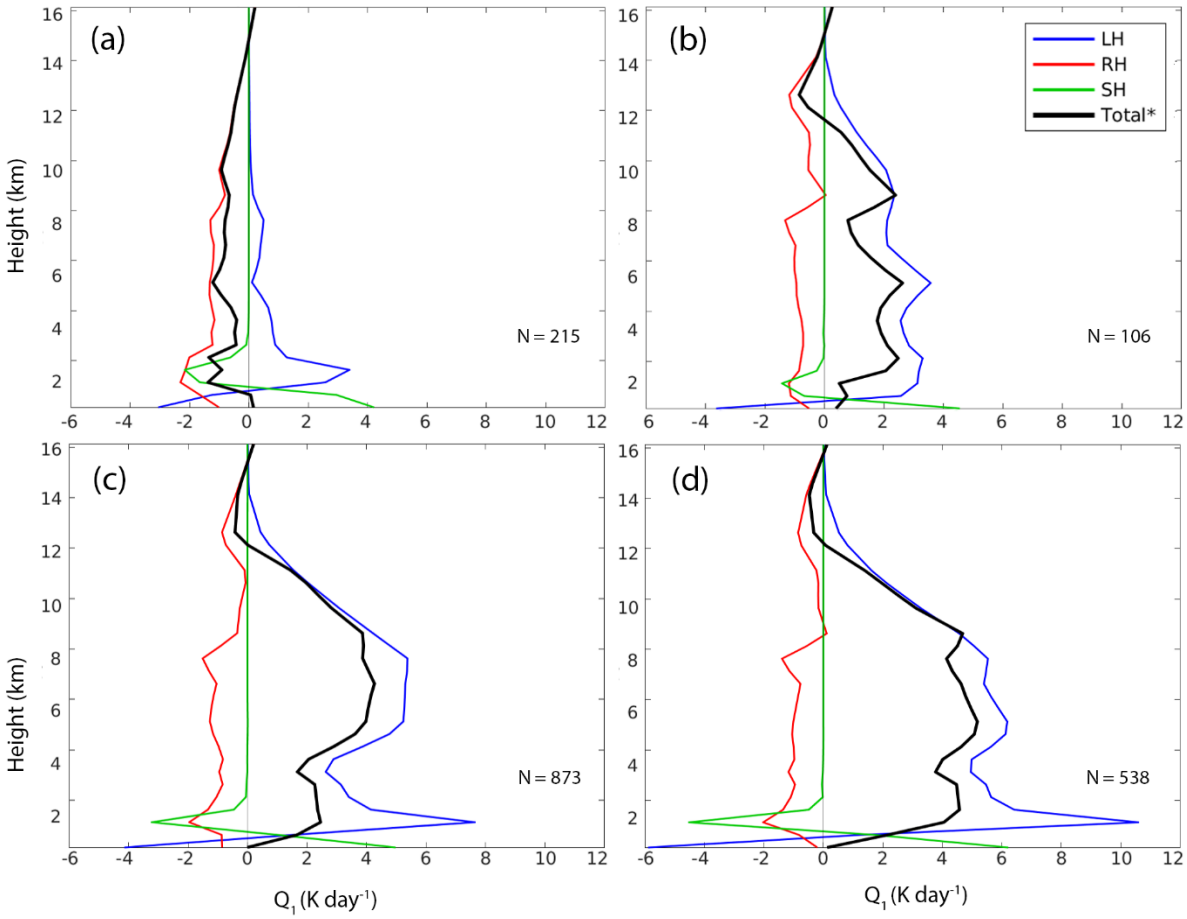

FIG. 2.12. Seasonality of NA conditional average heating profiles for 850 hPa waves in MERRA-2. All panels are for the year 2000 and represent (a) DJF, (b) MAM, (c) JJA, and (d) SON. The number of samples (*N*) is included in the bottom-right of each panel.

References

Belanger, J.I., Jelinek, M.T. and Curry, J.A., 2016: A climatology of easterly waves in the tropical Western Hemisphere. *Geosci. Data J.*, 3: 40-49.

Bellenger, H., Guilyardi, É., Leloup, J., Lengaigne, M., & Vialard, J., 2014: ENSO representation in climate models: From CMIP3 to CMIP5. *Climate Dynamics*, *42*(7), 1999-2018.

Berry, G. J., and C. D. Thorncroft, 2012: African easterly wave dynamics in a mesoscale numerical model: The upscale role of convection. *J. Atmos. Sci*., 69, 1267 1283

Burpee R. W., 1972: The origin and structure of easterly waves in the lower troposphere of North Africa. *J. Atmos. Sci.* 29:77–90.

Chen, T. C., Wang, S. Y., & Clark, A. J., 2008: North Atlantic hurricanes contributed by African easterly waves north and south of the African easterly jet. *Journal of Climate*, *21*(24), 6767-6776.

Cheng, Y., Thorncroft, C. D., & Kiladis, G. N., 2019: Two Contrasting African Easterly Wave Behaviors, *Journal of the Atmospheric Sciences*, *76*(6), 1753-1768.

Daloz, A. S., Chauvin, F., Walsh, K., Lavender, S., Abbs, D., & Roux, F., 2012: The ability of general circulation models to simulate tropical cyclones and their precursors over the North Atlantic main development region. *Climate dynamics*, *39*(7), 1559-1576.

Gelaro, R., and Coauthors, 2017: The Modern-Era Retrospective Analysis for Research and Applications, version 2 (MERRA-2). *J. Climate*, 30, 5419–5454.

Guo, Y., D. E. Waliser, and X. Jiang, 2015: A systematic relationship between activity of convectively coupled equatorial waves and the Madden-Julian oscillation in climate model simulations. *J. Climate*, 28, 1881-1904.

Hagos S, Zhang C, Tao W-K, Lang S, Takayabu YN, Shige S, Katsumata M, Olson B, L'ecuyer T., 2010. Estimates of tropical diabatic heating profiles: Commonalities and uncertainties. *J. Climate*. 23: 542–558.

Hartmann, D. L., H. H. Hendon, and R. A. Houze, 1984: Some implications of the mesoscale circulations in tropical cloud clusters for large-scale dynamics and climate. J. Atmos. Sci., 41, 113–121.

Henderson, S. A., E. D. Maloney, and E. A. Barnes, 2016: The influence of the Madden–Julian oscillation on Northern Hemisphere winter blocking. *J. Climate*, 29, 4597–4616.

Henderson, S. A., Maloney, E. D., & Son, S. W., 2017: Madden–Julian oscillation Pacific teleconnections: The impact of the basic state and MJO representation in general circulation models. *Journal of Climate*, *30*(12), 4567-4587.

Hodges, K. I., 1995: Feature tracking on the unit sphere. *Mon. Wea. Rev*., 123, 3458-3465.

Hollis, M., and Martin, E. R., "Development of a Global Tropical Wave Climatology." 34th Conference on Hurricanes and Tropical Meteorology (May 2021).

Houze, R. A., Jr., 1982: Cloud clusters and large-scale vertical motions in the Tropics. *J. Meteor. Soc. Japan*, 60, 396–410.

Houze, R. A. Jr., 1989: Observed structure of mesoscale convective systems and implications for large-scale heating. Quart. J. Roy. Meteor. Soc., 115, 425–461.

Hung, M., J. Lin, W. Wang, D. Kim, T. Shinoda, and S. Weaver, 2013: MJO and convectively coupled equatorial waves simulated by CMIP5 climate models. *J. Climate*, 26, 6185-6214.

Janiga, M. A., and C. D. Thorncroft, 2013: Regional differences in the kinematic and

thermodynamic structure of African easterly waves. *Quart. J. Roy. Meteor. Soc*., 139, 1598-1614.

Johnson, R. H., and P. E. Ciesielski, 2000: Rainfall and radiative heating rates from TOGA COARE atmospheric budgets. *J. Atmos. Sci.*, **57**, 1497–1514.

Knapp, K. R., M. C. Kruk, D. H. Levinson, H. J. Diamond, and C. J. Neumann, 2010: The International Best Track Archive for Climate Stewardship (IBTrACS). *Bull. Amer. Meteor. Soc.*, 91, 363–376.

Kummerow, C., and Coauthors, 2000: The Status of the Tropical Rainfall Measuring Mission (TRMM) after Two Years in Orbit. *J.* Appl. Meteor., **39**, 1965–1982.

Ladwig, W. C., & Stensrud, D. J., 2009: Relationship between tropical easterly waves and precipitation during the North American monsoon. *Journal of climate*, *22*(2), 258-271.

Lin, J. L., Kiladis, G. N., Mapes, B. E., Weickmann, K. M., Sperber, K. R., Lin, W., ... & Scinocca, J. F., 2006: Tropical intraseasonal variability in 14 IPCC AR4 climate models. Part I: Convective signals. *Journal of climate*, *19*(12), 2665-2690.

Lin, X., and R. H. Johnson, 1996: Heating, moistening and rainfall over the western Pacific during TOGA COARE. *J. Atmos. Sci.*, **53**, 3367–3383.

Ling, J., and C. Zhang, 2013: Diabatic Heating Profiles in Recent Global Reanalyses. *J. Climate*, 26, 3307-3325.

Lloyd, J., Guilyardi, E., & Weller, H., 2012: The role of atmosphere feedbacks during ENSO in the CMIP3 models. Part III: the shortwave flux feedback. *Journal of Climate*, *25*(12), 4275-4293.

Lubis, S. W., and C. Jacobi, 2015: The modulating influence of convectively coupled equatorial

waves (CCEWs) on the variability of tropical precipitation. Int. J. Climatol., 35, 1465–1483.

Madden, R. A., & Julian, P. R., 1971: Detection of a 40–50 Day Oscillation in the Zonal Wind in the Tropical Pacific, *J. Atmos. Sci.*, *28*(5), 702-708.

Malkus, J. S., 1962. Large scale interactions. The Sea, Vol. I. M.N. Hill, gen. ed. New York, John Wiley and Sons, 88-294.

Martin, E. R., & Thorncroft, C., 2015: Representation of African easterly waves in CMIP5 models. *Journal of Climate*, *28*(19), 7702-7715.

Matsuno, T., 1966: Quasi-geostrophic motions in the equatorial area. *J. Meteor. Soc. Japan*, 44, 25–43.

Matthews, A. J., 2004. Intraseasonal Variability over Tropical Africa during Northern Summer, *J. Climate*, 17(12), 2427-2440.

Norquist, D. C., E. E. Recker, and R. J. Reed, 1977: The energetics of African wave disturbances as observed during phase III of GATE. *Mon. Wea. Rev.,* 105, 334-342.

Park, M., & Lee, S., 2019: Relationship between Tropical and Extratropical Diabatic Heating and Their Impact on Stationary–Transient Wave Interference, *J. Atmos. Sci.*, 76(9), 2617-2633.

Pascale, S., & Bordoni, S., 2016: Tropical and extratropical controls of Gulf of California surges and summertime precipitation over the southwestern United States. *Monthly Weather Review*, *144*(7), 2695-2718.

Pasch, R. J., L. A. Avila, and J.-G. Jing, 1998: Atlantic tropical systems of 1994 and 1995: A comparison of a quiet season to a near-record-breaking one. *Mon. Wea. Rev.,***126,** 1106–1123.

Reed, R. J., & Recker, E. E., 1971: Structure and Properties of Synoptic-Scale Wave Disturbances in the Equatorial Western Pacific, *J. Atmos. Sci.,* 28 (7), 1117-1133.

Reed, R. J., Norquist, D. C., & Recker, E. E., 1977: The Structure and Properties of African Wave Disturbances as Observed During Phase III of GATE, *Monthly Weather Review, 105*(3), 317-333.

Riehl, H., and J. S. Malkus, 1958: On the heat balance in the equatorial trough zone. Geophysics, 6, 503-538.

Ryoo, J., Kaspi, Y., Waugh, D. W., Kiladis, G. N., Waliser, D. E., Fetzer, E. J., & Kim, J., 2013: Impact of Rossby Wave Breaking on U.S. West Coast Winter Precipitation during ENSO Events, *Journal of Climate*, *26*(17), 6360-6382.

Samanta, D., Karnauskas, K. B., Goodkin, N. F., Coats, S., Smerdon, J. E., & Zhang, L., 2018: Coupled model biases breed spurious low-frequency variability in the tropical Pacific Ocean. *Geophysical Research Letters*, *45*(19), 10-609.

Schlueter, A., Fink, A. H., Knippertz, P., & Vogel, P., 2019: A systematic comparison of tropical waves over northern Africa. Part I: Influence on rainfall. *Journal of Climate*, *32*(5), 1501-1523.

Schumacher, C., and R. A. Houze, 2000: Comparison of Radar Data from the TRMM Satellite and Kwajalein Oceanic Validation Site. J. Appl. Meteor., 39, 2151–2164.

Schumacher, C., R. A. Houze Jr., and I. Kraucunas, 2004: The tropical dynamical response to latent heating estimates derived from the TRMM Precipitation Radar, *J. Atmos. Sci*., 61, 1341-1358.

Schumacher, C., M. H. Zhang, and P. E. Ciesielski, 2007: Heating structures of the TRMM field campaigns. *J. Atmos. Sci.*, **64**, 2593–2610.

Schumacher, C., P. E. Ciesielski, and M. H. Zhang, 2008: Tropical cloud heating profiles: Analysis from KWAJEX. *Mon. Wea. Rev.*, **136**, 4289–4300.

Seo, K. H., & Son, S. W., 2012: The global atmospheric circulation response to tropical diabatic heating associated with the Madden–Julian oscillation during northern winter *J. Atmos. Sci.*, 69(1), 79-96.

Serra, Y.L., G.N. Kiladis, and M.F. Cronin, 2008: Horizontal and Vertical Structure of Easterly Waves in the Pacific ITCZ. *J. Atmos. Sci*., 65, 1266 1284.

Shige, S., Y. N. Takayabu, W. -K. Tao, and D. E. Johnson, 2004: Spectral retrieval of latent heating profiles from TRMM PR data. Part I: Development of a model-based algorithm, *J. Appl. Meteorol.,* 43, 1095-1113.

Shige, S., Y. N. Takayabu, S. Kida, W.-K. Tao, X. Zeng, and T. L'Ecuyer, 2009: Spectral retrieved of latent heating profiles from TRMM PR data. Part IV: Comparisons of lookup tables from two- and three-dimensional simulations, *J. Climate.*, 22, 5577–5594.

Skinner, C. B., & Diffenbaugh, N. S., 2013. The contribution of African easterly waves to monsoon precipitation in the CMIP3 ensemble. *Journal of Geophysical Research: Atmospheres*, *118*(9), 3590-3609.

Stachnik, J. P., and C. Schumacher, 2011: A comparison of the Hadley circulation in modern reanalyses. *J. Geophys. Res.*, **116**, D22102, doi:10.1029/2011JD016677.

Straub, K. H., & Kiladis, G. N., 2003: Interactions between the Boreal Summer Intraseasonal Oscillation and Higher-Frequency Tropical Wave Activity, *Monthly Weather Review, 131*(5), 945-960.

Tam, C.-Y., and T. Li, 2006: The origin and dispersion characteristics of the observed tropical

summertime synoptic-scale waves over the western Pacific. Mon. Wea. Rev., 134, 1630–1646.

Tao, W. K., S. Lang, J. Simpson, and R. Adler, 1993a: Retrieval algorithms for estimating the vertical profiles of latent heat release: Their applications for TRMM. *J. Meteor. Soc. Japan*, 71, 685–700.

Tao, W. K., and Coauthors, 2000: Vertical profiles of latent heat release and their retrieval in TOGA COARE convective systems using a cloud resolving model, SSM/I and radar data. *J. Meteor. Soc. Japan*, 78, 333–355.

Tao, W.-K., S. Lang, X. Zeng, S. Shige, and Y. Takayabu, 2010: Relating convective and stratiform rain to latent heating. *J. Clim.*, **23**, 1874–1893.

Tao, W. K., Y.N. Takayabu, S. Lang, S. Shige, W. Olson, A. Hou, G. Skofronick-Jackson, X. Jiang, C. Zhang, W. Lau, T. Krishnamurti, D. Waliser, M. Grecu, P.E. Ciesielski, R.H. Johnson, R. Houze, R. Kakar, K. Nakamura, S. Braun, S. Hagos, R. Oki, and A. Bhardwaj, 2016: TRMM Latent Heating Retrieval: Applications and Comparisons with Field Campaigns and Large Scale Analyses. *Meteorological Monographs*, 56, 2.1-2.34.

Thompson, R. M., Jr., S. W. Payne, E. E. Recker, and R. J. Reed, 1979: Structure and properties of synoptic-scale wave disturbances in the intertropical convergence zone of the eastern Atlantic. *J. Atmos. Sci.,* 36, 53–72.

Thorncroft, C., & Hodges, K., 2001: African easterly wave variability and its relationship to Atlantic tropical cyclone activity. *Journal of Climate*, *14*(6), 1166-1179.

Torres, V. M., C. D. Thorncroft, & N. M. J. Hall, 2021: Genesis of Easterly Waves over the Tropical Eastern Pacific and the Intra-Americas Sea, *J. Atmos. Sci.*, 78(10), 3263-3279.

Tulich, S. N., Kiladis, G. N., & Suzuki-Parker, A., 2011. Convectively coupled Kelvin and

easterly waves in a regional climate simulation of the tropics. *Climate dynamics*, *36*(1), 185-203.

Tyner, B., & Aiyyer, A., 2012: Evolution of African easterly waves in potential vorticity fields. *Monthly weather review*, *140*(11), 3634-3652.

Wheeler, M., and G. N. Kiladis, 1999: Convectively coupled equatorial waves: Analysis of clouds and temperature in the wavenumber–frequency domain. *J. Atmos. Sci*., 56, 374–399.

Wu, L., Z. Wen, R. Huang, and R. Wu, 2012: Possible linkage between the monsoon trough variability and the tropical cyclone activity over the western North Pacific. Mon. Wea. Rev., 140, 140–150,

Wu, X., Li, G., Jiang, W., Long, S. M., & Lu, B., 2021: Asymmetric relationship between ENSO and the tropical Indian Ocean summer SST anomalies. *Journal of Climate*, *34*(14), 5955-5969.

Yanai, M., S. Esbensen, and J.-H. Chu, 1973: Determination of bulk properties of tropical cloud clusters from large-scale heat and moisture budgets. *J. Atmos. Sci*., 30, 611 627.

Yang, G. Y., & Hoskins, B. J., 2016: ENSO-related variation of equatorial MRG and Rossby waves and forcing from higher latitudes. *Quarterly Journal of the Royal Meteorological Society*, *142*(699), 2488-2504.